Soil Dynamics and Earthquake Engineering 199 (2025) 109730

Contents lists available at ScienceDirect

Soil Dynamics and Earthquake Engineering

journal homepage: www.elsevier.com/locate/soildyn

Dynamic behavior and deformation of calcareous sand under cyclic loading

Bingxiang Yuan [a], Xianlun Huang [a], Runcheng Li [a], Qingzi Luo [a,*], Jim Shiau [b], Yonghong Wang [c], Junhong Yuan [d], Sabri Mohanad Muayad Sabri [e], Shiyuan Huang [f], Cheng Liao [g]

[a] School of Civil and Transportation Engineering, Guangdong University of Technology, Guangzhou, 510006, China
[b] School of Engineering, University of Southern Queensland, Toowoomba, QLD, 4350, Australia
[c] School of Civil Engineering, Qingdao University of Technology, Qingdao, 266520, Shandong, China
[d] School of Civil Engineering, Inner Mongolia University, Hohhot, 010070, China
[e] Peter the Great St. Petersburg Polytechnic University, St. Petersburg, 195251, Russia
[f] School of Materials Science and Engineering, Chongqing Jiaotong University, Chongqing, 400074, China
[g] Jiangxi Academy of Water Science and Engineering, Nanchang, 330029, China

ARTICLE INFO

Keywords:
Calcareous sand
Cyclic loading
Cumulative deformation
Triaxial test
Deviator stress

ABSTRACT

Calcareous sand undergoes substantial cumulative deformation under cyclic loading conditions, which may affect the safety and performance of marine structures exposed to wind and waves. To investigate this phenomenon, a series of drained cyclic triaxial tests were conducted on calcareous sand under varying confining pressures (σ_c), initial deviatoric stress ratios (η_s) and cyclic dynamic stress ratios (η_d). The results reveal that cumulative axial strain in calcareous sand increases with the number of loading cycles, while the rate of increase gradually diminishes, indicating a transition to a plastic stability stage. Most of the cumulative axial strain occurs within the first 100 cycles, with minimal incremental strain in subsequent cycles. Furthermore, the stress-strain curves become progressively denser as the number of cycles loading increases. Among the influencing factors, cyclic stress ratio and initial deviatoric stress ratio have a more significant effect on cumulative axial strain compared to confining pressure. Based on the experimental data, a model for predicting the cyclic cumulative deformation of saturated calcareous sand was developed. The model's predictions closely align with the experimental results, confirming its reliability. These findings enhance the understanding of cumulative deformation behavior in calcareous sand under cyclic loading and provide valuable insights for the design and maintenance of marine infrastructure.

1. Introduction

Calcareous sand, widespread presence in the South China Sea, is seeing increased attention due to the rapid development of coastal engineering projects in the area. Consequently, research on calcareous sand materials has drawn the attention of numerous scholars [1–4].

Calcareous sand and silica sand exhibit significant differences in their physical and mechanical properties due to variations in mineral composition and particle structure. Notably, calcareous sand is characterized by an irregular particle shape, a rough surface, and considerably lower particle strength compared to silica sand [5–8]. As a vital geotechnical material, calcareous sand plays a critical role in island constructions, particularly in the design of submarine roadbeds and piles for coastal regions and offshore oilfields [9–11].

In marine engineering, calcareous sand is continually exposed to cyclic loads generated by waves and wind over tens of thousands of cycles. These loads are typically characterized by low cyclic stress and low-frequency horizontal forces [12]. The effects of cyclic loading can lead to cumulative deformation within calcareous sand; such deformations may persist even after millions of cycles have occurred [13]. These cumulative deformations pose severe implications for the normal operation of marine infrastructure [14,15], potentially resulting not only in engineering failures but also incurring substantial economic losses [16,17]. Therefore, investigating the mechanisms underlying cumulative deformation in calcareous sand and establishing a long-term model for such deformations are critically important for advancing offshore engineering practices.

It is important to comprehend the mechanical properties of

---

* Corresponding author.
E-mail address: lqz1986@gdut.edu.cn (Q. Luo).

https://doi.org/10.1016/j.soildyn.2025.109730
Received 7 January 2025; Received in revised form 11 August 2025; Accepted 11 August 2025

calcareous sand for the purposes of foundation design and evaluating disaster risk. In recent years, extensive research has been conducted on the mechanical properties of calcareous sand, often utilizing static and dynamic triaxial tests as well as cyclic ring shear tests [12,18–20]. Among these, the triaxial test is one of the most effective and commonly used methods for studying calcareous sand. This test not only provides key mechanical parameters of the material but also enables the observation of failure modes in calcareous sand. Analysis of the resulting data can reveal critical properties such as strength and deformation behavior [21–24].

With the deepening of research on calcareous sand, it has been discovered that various factors such as grain size [25], drainage conditions [26], relative density [27], cyclic stress ratio [14], and cyclic frequency [28] have substantial influences on the deformation behavior of calcareous sand. He et al. [29] carried out long-term cyclic dynamic triaxial tests on compact calcareous sand under drained conditions to investigate the characteristics of accumulated permanent deformation at various loading frequencies and dynamic stress levels. The study revealed that the accumulated axial strain of calcareous sand diminishes as increasing confining pressure, and an increase in loading frequency would lead to an increase in the limiting strain. Moreover, the study demonstrated that the axial deviatoric stress had a more prominent influence on the accumulated deformation of calcareous sand than confining pressure and stress level.

Wang et al. [30] discovered that as the cyclic stress ratio increased, the axial plastic strain also ascended. However, both the axial plastic strain and the initiation of grain crushing initially increased and then stabilized. Although calcareous sand possesses certain crushing potential [31], there is also a stress threshold for the crushing of calcareous sand. Salem et al. [18] noted that in the monotonic and cyclic unconfined triaxial tests carried out at low stress levels, the amount of grain crushing was extremely small and negligible. Wang et al. [32] further affirmed in their research concerning the characteristics of particle damage under triaxial shear that at lower confining pressures (50–200 kPa), the size of the original particles remains essentially unaltered. Additionally, they declared that the particle breakage induced by cyclic shearing is significantly less than that caused by monotonic shearing until failure.

Furthermore, with respect to the study on the deformation patterns of calcareous sand, He et al. [14] indicated that a significant correlation exists between the loading stress path (LSP) and the development of cumulative axial strain. They also maintained that the mechanical behavior of calcareous sand at low stress levels is predominantly influenced by the stress path and the stress level.

Although extensive research has been conducted on the mechanical and accumulated permanent deformation properties of calcareous sand, its mechanical and deformation behavior is significantly influenced by variations in particle arrangement and stress history. These differences are largely attributed to the disparities in the original and depositional environments [33]. However, research on the impact of stress path on the cumulative deformation of calcareous sand remains relatively limited. Therefore, further studies are essential to explore how stress path influences the cumulative deformation of calcareous sand under long-term cyclic loading. Such investigations are crucial for enhancing the safety and reliability of infrastructure in complex marine environments.

Due to its distinctive characteristics, such as sharp edges and rough surfaces, calcareous sand exhibits more complex shear behavior compared to silica sand [34,35]. Additionally, calcareous sand is more sensitive to confining pressure and demonstrates smaller elastic deformation than silica sand [36]. While numerous studies have examined the deformation of silica sand under cyclic loading, research on calcareous sand in this context remains relatively limited, particularly regarding the development of cumulative deformation prediction models. Given the critical importance of cumulative deformation in the engineering design of calcareous sand structures [37], it is essential to establish a robust mathematical model for accurately predicting cumulative deformation under cyclic loading.

To address the need for predicting long-term cumulative strain in calcareous sand, scholars have proposed various constitutive models. For instance, Monismith et al. [38] first established the relationship model between cycle numbers and soil cumulative deformation. Li and Selig [39] proposed improved formulations considering the magnitude effects of cyclic loading. Building upon these foundations, Chai et al. [40] incorporated additional consideration of deviatoric stress effects. He et al. [41] integrated the influence of relative stress states to reformulate the cumulative strain model. Yesuf et al. [42] investigated the influence of initial plastic deformation using the Drucker-Prager yield criterion, and developed a cumulative strain prediction model, with parameters optimized through iterative validation.

Jafarian et al. [43] highlighted the impact of initial stress anisotropy on the dynamic behavior of calcareous sand and introduced a modified factor based on stress anisotropy to develop a constitutive model. Lu et al. [44] later proposed the concept of characteristic stress and developed a 3D fractional elasto-plastic constitutive model that effectively accurately predicts strength and deformation behavior of soil. Building on this, Liu et al. [45] defined yield surface shape parameters using a new hardening rule with unified parameters. By conducting triaxial compression tests on calcareous sand with varying densities, they developed a plastic constitutive model incorporating relative density.

Wang et al. [30], based on the principle of stability, proposed a critical stress formula to predict the stress-strain behavior of calcareous sand under cyclic loading. Additionally, Zhang et al. [46] performed monotonic shear tests for calcareous sand and devised a physically meaningful mathematical model for describing the monotonic stress-strain relationship. Their model, based on confining pressure and relative density, employed hyperbolic functions and an inverted S-shaped function enhanced accuracy. To investigate the deformation effects of cyclic loading on calcareous sand, Wang and Zhang [47] extended Zhang's earlier work by incorporating the cyclic power ratio and loading frequency. They proposed a prediction formula based on hyperbolic functions, to estimate the permanent deformation of calcareous sand under cyclic loading. Through a series of undrained cyclic triaxial tests, Ma et al. [48] decomposed the axial strain of saturated calcareous sand into residual and cyclic components, demonstrated that the consolidation ratio and cyclic stress ratio govern the deformation pattern, and proposed an empirical model. Similarly, Peng et al. [49] established a dilatancy equation that accounts for the effects of consolidation stress and stress path on dilatant behavior, stress-strain response, and particle breakage, providing a framework to characterize and simulate the volumetric deformation behavior of materials under varying stress paths. The high-cycle accumulation (HCA) model proposed by Niemunis et al. [50]. Drawing on laboratory tests with glass beads, natural sand, and quartz sand, Wichtmann [51] subsequently extended the model by introducing an improved pressure function and deriving quantitative relationships between grain shape and the parameters C_{ampl}, C_p, and C_Y.

Despite these advancements, as shown in Table 1, a dedicated model for predicting the long-term cumulative deformation of calcareous sand under varying stress history conditions remains lacking. Consequently, the theoretical development and establishment of a predictive model for the cumulative deformation characteristics of calcareous sand under cyclic loading with multiple consolidation states is a pressing issue. Building on this premise, the present study conducted cyclic triaxial shear tests on saturated calcareous sand under drainage conditions, focusing on coral reef engineering in the South China Sea. The research investigated the effects of factors, such as confining pressure, consolidation conditions, and dynamic-to-static deviatoric stress ratios, on the cumulative deformation behavior of calcareous sand, exploring the mechanisms underlying these influencing factors. Based on the experimental findings, a mathematical model was developed to predict the cumulative deformation of saturated calcareous sand, with

Table 1
Summary of Cumulative deformation formula and Correlation formula in the literature.

No.	Relationship	Soil type	Model Formula	Reference
1	ε_N - N	Silty clay	$\varepsilon_N = AN^b$	Monismith et al. (1975) [38]
2	ε_N - $N, \frac{\sigma_d}{\sigma_s}$	Fine-grained soil	$\varepsilon_N = a\left(\frac{\sigma_d}{\sigma_s}\right)^m N^b$	Li and Selig (1996) [39]
3	ε_N - N, q_d, q_s	Soft soil	$\varepsilon_N = a\left(\frac{q_d}{q_f}\right)^m \left(1+\frac{q_s}{q_f}\right)^n N^b$	Chai et al. (2002) [40]
4	D^{acc} - N, e, p_s	Medium coarse uniform sand	$D^{acc} = mf_{ampl}\dot{f}_N f_p f_Y f_e f_\pi$	Niemunis et al. (2005) [50]
5	ε_N - $N, \frac{\sigma_d}{q_s}$	Fine-grained soil	$\varepsilon_N = \sum_{N=1}^{N}\left(N^{m^{\left(1-\frac{\sigma_d}{q_s}\right)}}\right)\varepsilon_{p1,0};$ $\varepsilon_{p1} = \alpha_1 N^{\alpha_2}\left(\frac{\sigma_{oct}}{P_{ref}}\right)^{\alpha_3}\left(\frac{\tau_{oct}}{P_{ref}}\right)^{\alpha_4}$	Yesuf et al. (2015) [42]
6	ε_N - N, p_s	Calcareous sand	$\varepsilon_N = a(D^*)m\left(\frac{p_s}{p_a}\right)^c N^b$	He et al. (2019) [41]
7	ε_N -e_0, κ, λ	Fujinomori clay	$\varepsilon_N = \frac{\lambda-\kappa}{\beta(1+e_0)}\ln\frac{c_{nx}}{c_{n0}}$	Lu et al. (2019) [44]
8	$\dot{\varepsilon}_N$ - N, e, p_s	Quartz sand	$\dot{\varepsilon}_N = f_{ampl}\dot{f}_N f_e f_p f_Y f_\pi$	Wichtmann et al. (2019) [51]
9	ε_p - φ, σ_3	Calcareous sand	$\varepsilon_p = \frac{2a(c\cdot\cos\varphi+\sigma_3\cdot\sin\varphi)}{1-\sin\varphi-2b(c\cdot\cos\varphi+\sigma_3\cdot\sin\varphi)}$	Zhang et al. (2020) [46]
10	χ_0 - B_r, p_a	Calcareous sand	$\chi_0 = 1-\left(\left(\frac{\lambda_c-\kappa}{\lambda_r-\kappa}+\frac{bB_r}{\lambda_r-\kappa}\left(\frac{p_a}{p_0}\right)^{\xi}\right)^{\frac{1}{\xi}}-1\right)^{-\frac{1}{2}}$	Liu et al. (2021) [45]
11	ε_{ult}^{N} - q_d, σ_3	Calcareous sand	$\varepsilon_{ult}^{N} = a^*\left(\frac{q_d}{\sigma_3}\right)^b$	Wang et al. (2022) [52]
12	$d - e, B_r$	Calcareous sand	$d = A_d\left(M_{cs}e^{k_d}\left[e-e_0+\alpha\left(\frac{p'}{P_a}\right)^{0.44}+\chi\ln(B_r)\right]\right)-\eta\left(\frac{\eta}{M_{cs}}e^{k_d}\left[e-e_0+\alpha\left(\frac{p'}{P_a}\right)^{0.44}+\chi\ln(B_r)\right]\right)$	Peng et al. (2023) [49]
13	ε_N - N, e, p_s	Calcareous sand	$\varepsilon_p = a_1\left(e^{a_2 N/N_i}-1\right)+a_3 b_1\left(\frac{N}{N_f}\right)^{b_2}$	Ma et al. (2024) [48]

Notes: ε_N is cumulative strain, ε_N^{ult} is ultimate cumulative strain, ε_p is critical strain, $\dot{\varepsilon}_N$ is strain rate, σ_d is dynamic stress, σ_s is static stress, q_s is initial deviatoric stress, q_d is the amplitude of cyclic stress, p_s is mean effective stress, D^{acc} is accumulation rate, e_0 is initial porosity, κ is swelling index, λ is compression index, χ_0 is the ultimate degree of particle breakage, B_r is relative breakage index, d is dilatancy ratio.

corresponding model parameters provided. A comparison of the model's predictions with experimental results. Confirmed its validity. The model established in this study offers robust support for engineering design and construction practices, particularly for projects involving calcareous sand.

2. Test materials and methods

2.1. Test materials

The calcareous sand samples used in this study were obtained from the Xisha Islands of the South China Sea, primarily constituted by marine bioclastic sediments with calcium carbonate ($CaCO_3$) as the dominant mineral component. Table 2 presents the basic properties of the calcareous sand, which differs from standard sand due to its notably higher internal friction angle and distinct cohesion.

Existing research has shown that the friction angle of calcareous sand typically ranges from 1.1 to 1.3 times that of silica sand, and its cohesion is approximately 1.5–2 greats than of silica sand [35]. Scanning electron microscopy (SEM) images of the calcareous sand, shown in Fig. 1, reveal that the particles are angular and irregular in shape, with an exceptionally rough surface and numerous internal pores, resulting from the corrosion of the original biological skeleton. Fig. 2 presents the particle size distribution and gradation curve of the calcareous sand, indicating that the majority of the particles (over 80 %) fall within the size range of 0.3–1.18 mm. In contrast, the number of particles larger than 2 mm and smaller than 0.075 mm are relatively scarce. Analytical calculations show that the uniformity coefficient (C_u) of the calcareous sand in this study is 1.034, and the curvature coefficient (C_c) is 2.604, indicating poor gradation.

Table 2
Physical and mechanical parameters of the calcareous sand.

Property	Calcareous sand
Density (ρ)	1.451 g/cm^3
Particle Density (G_s)	2.82
Maximum dry density (ρ_{max})	1.610 g/cm^3
Minimum dry density (ρ_{min})	1.320 g/cm^3
Internal frictional angle (φ)	40.850°
Cohesion (c)	13.060 kPa
60 % passing grain size (d_{60})	0.326
30 % passing grain size (d_{30})	0.205
10 % passing grain size (d_{10})	0.125

2.2. Sample preparation and test procedures

The triaxial cyclic loading tests in this study were conducted using the SPAX-2000 (GCTS Testing Systems Ltd., USA), with its key components illustrated in Fig. 3(a). The system configuration comprises: (1) Cell Pressure Intensifier: Controls and amplifies the confining pressure applied to the soil sample in the triaxial cell. (2) Triaxial Cell: The central testing chamber that houses the soil specimen, where the sample is placed and subjected to controlled stress conditions. (3) Digital Controller: The electronic control unit that manages test parameters including stress paths and loading rates. (4) Computer: Handles data acquisition, storage, and analysis. (5) Hydraulic Pump: Generates the hydraulic pressure needed to power the loading systems.

The testing procedure was divided into four main steps: (1) Sample preparation by sand pluviation method: A sand pourer device was used to prepare the samples with a relative density of 50 %. The sand flow

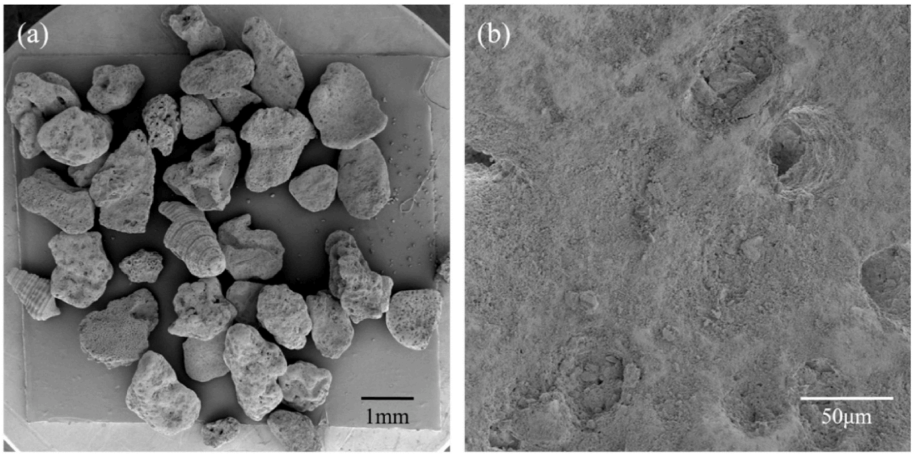

Fig. 1. Scanning electron microscopy images of the calcareous sand sample (a) Multiple particle image (b) Single particle image.

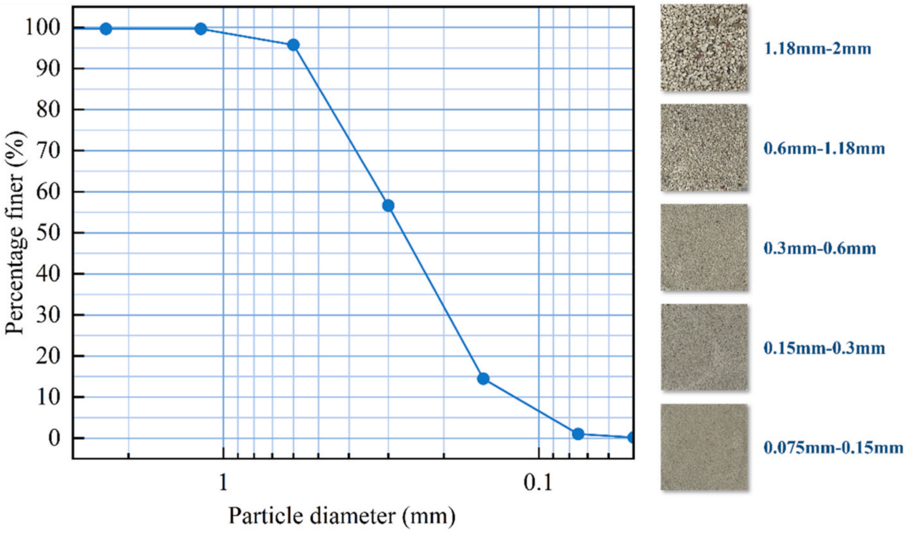

Fig. 2. Particle size distribution and grading curve of the tested calcareous sand samples.

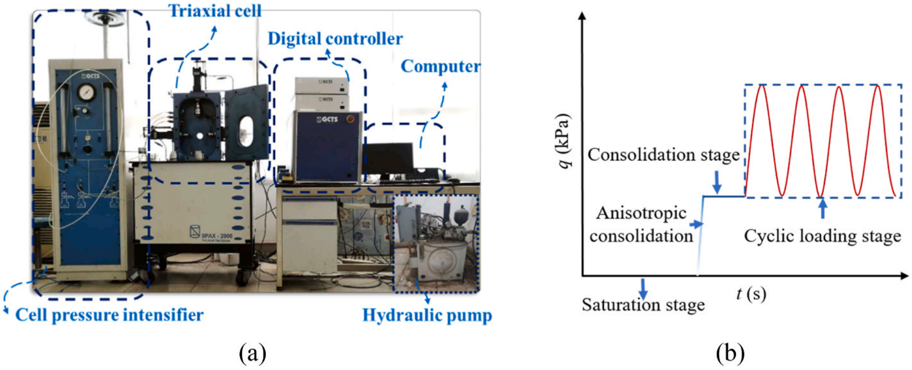

Fig. 3. Experimental systems and loading diagram (a) Soil poly-axial test systems (b) Loading stress path.

rate was controlled at 105 g/s, and the falling height was maintained at 150 cm. The sample dimensions were rectangular measuring 120 mm × 50 mm × 50 mm. (2) Saturation: Back pressure was applied to the specimen, increasing at a rate of 1 kPa/s until reaching and maintaining 140 kPa. The back pressure forces distilled water to permeate the specimen, expelling gas. Saturation was considered complete when the measured pore pressure reached the target value of $B = \frac{\Delta u}{\Delta \sigma_c} \geq 95\%$. (3) Consolidation: Following the application of confining pressure to the saturated specimen, the relationship curve between drainage volume and the square root of time was recorded. Consolidation was deemed complete when the measured pore pressure equalled the initial pore pressure and the drainage volume stabilized. Two distinct methods were used to assess the effects of consolidation state: deviatoric stress consolidation and deviatoric stress consolidation following isobaric consolidation. The former required approximately 6 h, while the latter took approximately 4 h (4) Loading: To simulate the combined effects of wave loads and wind, cyclic triaxial consolidated-drained tests were performed after specimen consolidation. Stress-controlled loading was applied with a 0.5 Hz sinusoidal wave (Fig. 3(b)). The loading pattern followed the expression shown in Eq. (1) [6], and the test was terminated after 5000 cycles.

$$q_{cyc} = q_d \frac{1 + \sin\left(\omega t - \frac{\pi}{2}\right)}{2} \tag{1}$$

where q_{cyc} is the cyclic load, q_d is the amplitude of cyclic stress, ω is the angular frequency (with a value of π when the frequency is 0.5 Hz), and t is the cyclic loading time.

2.3. *Definitions of stress, strain*

The mean effective stress p_s and the initial deviatoric stress q_s are calculated using Eqs. (2) and (3), respectively.

$$p_s = \frac{\sigma_{1s} + 2\sigma_{3s}}{3} \tag{2}$$

$$q_s = \sigma_{1s} - \sigma_{3s} \tag{3}$$

where σ_{1s} and σ_{3s} are the major and minor principal stress, respectively.

The initial deviatoric stress ratio (η_s) and the cyclic stress ratio (η_d) are defined by Eqs. (4) and (5), as follows:

$$\eta_s = \frac{q_s}{p_s} \tag{4}$$

$$\eta_d = \frac{q_d}{p_s} \tag{5}$$

Fig. 4 illustrates axial strain versus cycle number under cyclic loading, where the total axial strain ε comprises accumulated axial plastic strain ε_p and elastic strain ε_e, as shown in Eq. (6):

$$\varepsilon_a = \varepsilon_p + \varepsilon_e \tag{6}$$

2.4. *Testing program*

The study examined the effects of confining pressure (σ_c), initial deviatoric stress ratio (η_s), and cyclic stress ratio (η_d) on cumulative deformation of calcareous sand. As stated in Indraratna [53], cyclic triaxial tests are widely used to analyze the drainage behavior of geotechnical materials under long-term cyclic loading. To investigate the mechanical response of calcareous sand under cyclic loading, 27 comparative consolidated-drained cyclic triaxial tests were conducted.

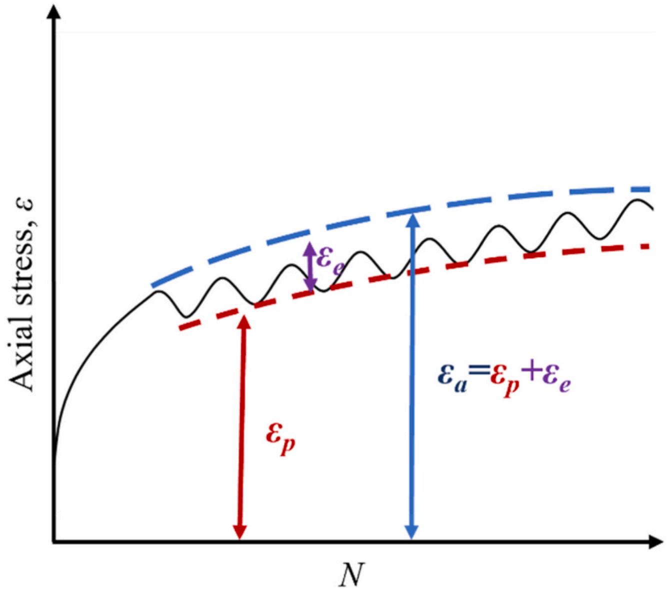

Fig. 4. The axial strain versus number of cycles under cyclic loading.

The specific test scheme is provided in Table 3. The experimental samples are labeled using the format "CD-c-s-d", where the components of the label represent the following: "CD" denotes the drainage condition, "c" represents the specific confining pressure (σ_c), "s" denotes the initial deviatoric stress ratio (η_s), and "d" denotes the cyclic stress ratio (η_d). For example, "CD-100-0-0.2″ indicates an experimental setup with the drainage condition applied, a confining pressure (σ_c) of 100 kPa, an initial deviatoric stress ratio (η_s) of 0, and a cyclic stress ratio (η_d) of 0.2.

Table 3
The cyclic triaxial experimental program.

No.	σc (kPa)	ηs	σ1c (kPa)	ps (kPa)	qs (kPa)	ηd	qd (kPa)
CD-100-0-0.2	100	0	100	100.00	0	0.2	20
CD-100-0-0.4	100	0	100	100.00	0	0.4	40
CD-100-0-0.6	100	0	100	100.00	0	0.6	60
CD-100-0.2-0.2	100	0.2	121.4	107.13	21.4	0.2	21.4
CD-100-0.2-0.4	100	0.2	121.4	107.13	21.4	0.4	42.8
CD-100-0.2-0.6	100	0.2	121.4	107.13	21.4	0.6	64.3
CD-100-0.4-0.2	100	0.4	146.1	115.37	46.2	0.2	23.1
CD-100-0.4-0.4	100	0.4	146.1	115.37	46.2	0.4	46.2
CD-100-0.4-0.6	100	0.4	146.1	115.37	46.2	0.6	69.2
CD-200-0-0.2	200	0	200	200.00	0	0.2	40
CD-200-0-0.4	200	0	200	200.00	0	0.4	80
CD-200-0-0.6	200	0	200	200.00	0	0.6	120
CD-200-0.2-0.2	200	0.2	242.8	214.27	42.8	0.2	42.8
CD-200-0.2-0.4	200	0.2	242.8	214.27	42.8	0.4	85.7
CD-200-0.2-0.6	200	0.2	242.8	214.27	42.8	0.6	128.5
CD-200-0.4-0.2	200	0.4	292.2	230.73	92.3	0.2	46.2
CD-200-0.4-0.4	200	0.4	292.2	230.73	92.3	0.4	92.3
CD-200-0.4-0.6	200	0.4	292.2	230.73	92.3	0.6	138.5
CD-300-0-0.2	300	0	300	300.00	0	0.2	60
CD-300-0-0.4	300	0	300	300.00	0	0.4	120
CD-300-0-0.6	300	0	300	300.00	0	0.6	180
CD-300-0.2-0.2	300	0.2	364.2	321.40	64.3	0.2	64.3
CD-300-0.2-0.4	300	0.2	364.2	321.40	64.3	0.4	128.5
CD-300-0.2-0.6	300	0.2	364.2	321.40	64.3	0.6	192.8
CD-300-0.4-0.2	300	0.4	438.3	346.10	138.5	0.2	69.2
CD-300-0.4-0.4	300	0.4	438.3	346.10	138.5	0.4	138.5
CD-300-0.4-0.6	300	0.4	438.3	346.10	138.5	0.6	207.7

3. Experimental observations and interpretations

3.1. Cumulative axial strain

Fig. 5 illustrates the development of cumulative axial strain of the specimen with increasing cycle numbers. The subsequent discussion would focus on the experimental results under the loading conditions of $\sigma_c = 300$ kPa and $\eta_s = 0.4$. From Fig. 5(a), it can be observed that under different cyclic stress ratios (η_d), the development trend of cumulative axial strain (ε_p) with respect to the number of cycles loading is essentially consistent. Specifically, the cumulative axial strain (ε_p) increases continuously with the increasing number of cycles, and the rate of increase decreases over time. In the first 10 cycles, the strain accumulated rapidly, accounting for approximately 70 % of the final cumulative strain. In contrast, during the last 10 cycles, the cumulative strain remained nearly unchanged, and the strain rate approached zero.

Fig. 5(b) shows that the cumulative axial strain rate ε_p (% per second) is comparatively high in the initial stage. With the increase of loading cycles number, the cumulative axial strain rate gradually diminishes, eventually approaching zero. Notably, the most significant reduction in the cumulative axial strain rate occurs within the 10th cycle. Furthermore, the rate of decay accelerates as the cyclic stress ratio decreases. For instance, when the $\eta_d = 0.6$, 0.4, and 0.2, the cumulative axial strain rates for the first load cycle are 1.18, 0.87, and 0.4, respectively. By the 10th cycle, these rates have decreased to 0.21, 0.12, and 0.01, representing decay rates of 82.2 %, 86.2 %, and 97.5 %, respectively. In the later stages of loading (after 100th cycle), the cumulative axial strain rate gradually stabilizes and approaches zero, indicating that the deformation has reached a stable state.

The shakedown theory is primarily used to analyze and assess the behavior of structures under cyclic loading. It is widely applied to explain the strain development of soil under cyclic loading [54,55]. Based on the distinct cumulative deformation response patterns of soil, the shakedown theory categorizes the cumulative deformation behavior into three categories: plastic shakedown, plastic creep, and incremental plastic failure (Fig. 6).

As shown in curve (a) in Fig. 6, plastic shakedown occurs when soil experiences limited plastic deformation during initial loading cycles. With continued cyclic loading, however, the plastic deformation gradually stabilizes. This behavior typically occurs in specimens subjected to relatively low loading magnitudes and favorable drainage conditions [30]. In contrast, under poor drainage conditions and appropriate cyclic loading intensities, soil may experience deformation accumulation over time due to internal plastic flow, a phenomenon termed plastic creep, as shown in curve (b) in Fig. 6. Shiau pointed out that under cyclic loading, there exists a “stability limit load” beyond which irreversible incremental plastic failure will occur [56]. When drainage conditions are insufficient and applied loads exceed this stability limit, soil undergoes irrecoverable plastic deformation during each loading cycle. These deformations progressively accumulate with repeated loading, ultimately leading to structural instability or failure, as depicted in curve (c) in Fig. 6.

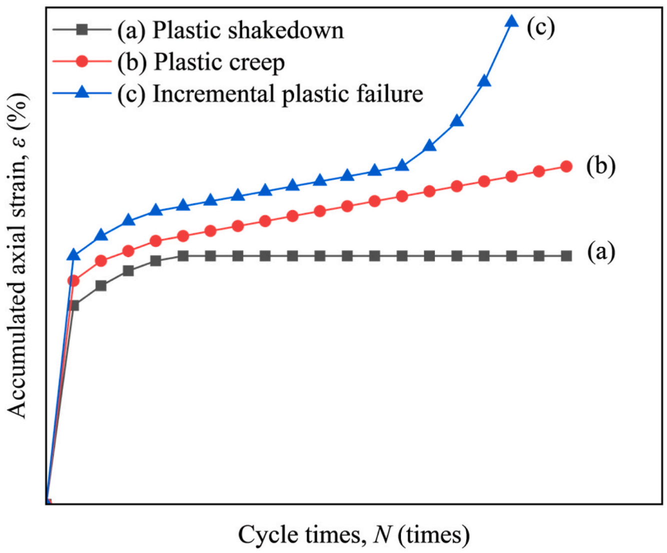

Fig. 6. Stability theory behavior classification.

From the experimental results presented in Fig. 5, it is evident that during the initial loading phase, calcareous sand accumulates a certain amount of plastic deformation. However, as the number of loading cycles increases, the rate of plastic strain rapidly decreases to a lower level. Ultimately, the deformation response tends toward elasticity, similar to the behavior observed in curve (a) of Fig. 6, which is used to describe the plastic shakedown of soil. This behavior can be attributed to the relatively high permeability coefficient of calcareous sand [57], and since all experiments in this study were conducted under drained boundary conditions, the soil specimens exhibit plastic shakedown rather than plastic creep failure. Curve (a) in Fig. 6 further illustrates that once calcareous sand reaches the plastic shakedown state, the accumulated axial strain becomes stable and controllable, with no sudden large deformations occurring. This behavior is advantageous for practical engineering applications.

3.2. Deviatoric stress-strain

Fig. 7 illustrates the deviatoric stress-strain relationship for calcareous sand with confining pressure $\sigma_c = 300$ kPa, initial deviatoric stress

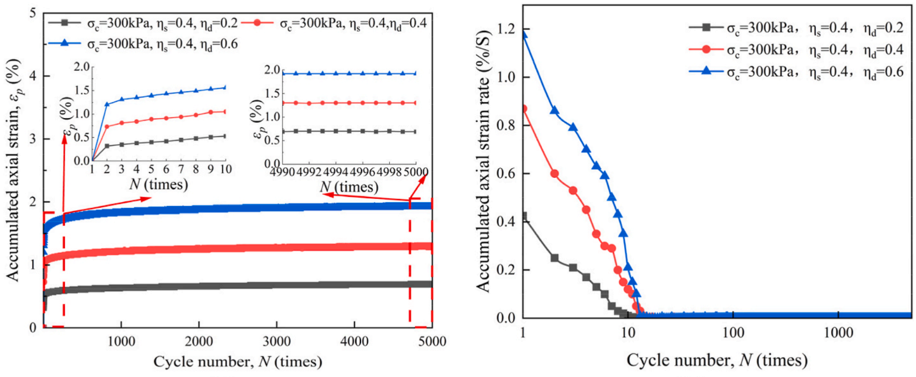

(a) (b)

Fig. 5. Cumulative axial strain development trends (a) Relationship between cumulative axial strain and number of cycles (b) Relationship between cumulative axial strain rate and number of cycles.

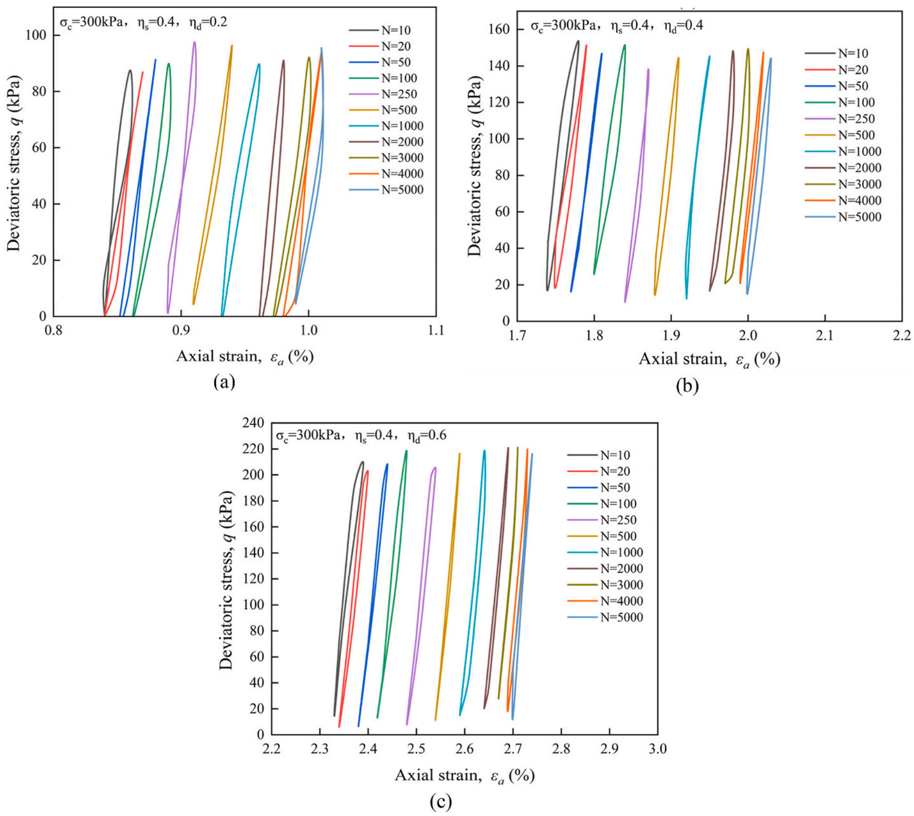

(a) (b) (c)

Fig. 7. Deviatoric stress-strain relationship curve: σ_c = 300 kPa, η_s = 0.4, (a) η_d = 0.2 (b) η_d = 0.4 (c) η_d = 0.6.

ratio $\eta_s = 0.4$, and cyclic stress ratios $\eta_d = 0.2$, 0.4, 0.6. As shown, the hysteresis loops consistently shift towards higher axial strain with an increasing number of cycles, indicating the accumulation of axial strain. Initially, the hysteresis loops are widely spaced; however, with the increase in cycle loading numbers, the rate of axial strain growth in calcareous sand decreases, leading to more compact hysteresis loops and a reduction in the loop area. This phenomenon is attributed to the rough surface and intricate particle morphology of calcareous sand [58]. Under deviatoric stress, the sample initially undergoes reorganization and potential particle fragmentation [36]. With further cycling, the rate of plastic strain growth in calcareous sand stabilizes, and the sample reaches a steady state where particle arrangements become more stable, resulting in tighter deviatoric stress-strain relationships and even curve overlap. This occurs for the various cyclic stress ratios ($\eta_d = 0.2$, 0.4, 0.6) considered in this study.

Noting that the hysteresis loop represents the area enclosed by the hysteresis curve of calcareous sand, its size decreases as the number of cyclic loading increases. The reduction in the hysteresis loop area indicates a decline in the elastic properties of the soil [59]. By integrating the individual hysteresis loops in Fig. 7 to calculate their respective areas S, it becomes clear that the area of the hysteresis loop for the 100th cycle is significantly larger than that of the 5000th cycle. For instance, when $\sigma_c = 300$ kPa, $\eta_s = 0.4$, and $\eta_d = 0.2$, 0.4, 0.6, the areas corresponding to the 5000th cycle of the samples are 48.19 %, 65.90 %, and 77.51 % of the area measured at the 100th cycle, respectively. This indicates that S_{100} is greater than S_{5000}. The changes in the area of the hysteretic loop from the 100th to the 5000th cycle are 51.81 %, 34.10 %, and 22.49 %, respectively.

It is to be noted that the change for the area of the hysteresis loop S decreases as the cyclic stress ratio (η_d) increases (see Fig. 7). Specifically, the change in the hysteretic loop area is more pronounced during the initial 100th cycle under higher cyclic stress conditions, suggesting that the degradation of the soil's elastic properties is concentrated in the early stages. Consequently, cyclic stress significantly influences the stability of calcium sand under long-term cyclic loading. Furthermore, when 5000th cycle, the change in both elastic and plastic deformation of the soil approach zero, and the sample achieves a high level of stability, indicating that calcium sand exhibits strong resistance to deformation under long-term cyclic loading. This finding is of considerable importance for engineering structures, such as offshore piles, that are subject to long-term cyclic loading.

3.3. *Cumulative volumetric strain*

The volume deformation of sandy soil is influenced by the drainage of pore water and the rearrangement and redistribution of grain particles [60,61]. Fig. 8(a) illustrates the relationship between cumulative volumetric strain and the number of cycles loading, showing that as the number of cycles loading increases, the rate of change in the cumulative volumetric strain of calcareous sand gradually decreases. Under the loading conditions of $\sigma_c = 300$ kPa and $\eta_s = 0.4$, when the cyclic stress ratio $\eta_d = 0.6$, 0.4, and 0.2, the cumulative volumetric strain at the 10th cycle accounts for 58.82 %, 55.95 %, and 48.59 % of the final cumulative volumetric strain, respectively. According to the measured pore pressure results during the experiment, the pore water pressure in calcareous sand is largely dissipated after the 10th cycle, and subsequent cyclic accumulated pore water pressure changes are negligible, consistent with the findings of Zhang et al. [27]. At this stage, the change in volumetric strain is primarily due to the combined effects of pore water drainage and grain rearrangement, with the volumetric strain caused by pore water drainage being predominant. However, the volumetric strain from the 10th cycle to the 100th cycle is 9.76 %, 11.20 %, and 10.07 %, which is relatively insignificant compared to the volumetric strain from the 10th cycle to the 5000th cycle. This is mainly because, under long-term cyclic loading conditions after the 10th cycle, the volume deformation of calcareous sand is primarily due to the rearrangement

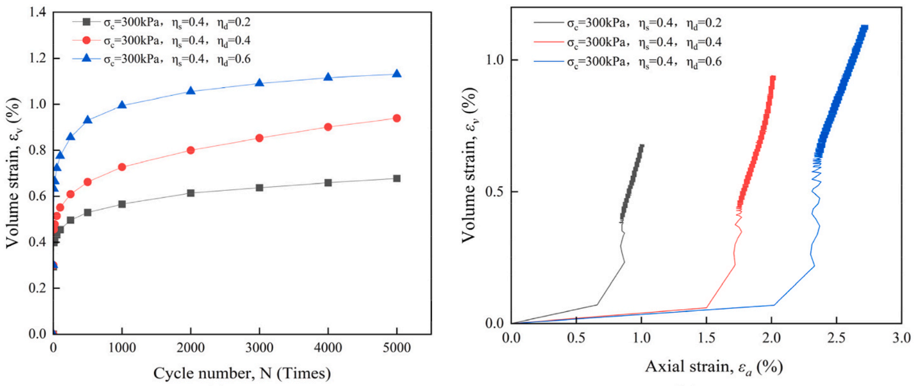

(a) (b)

Fig. 8. Development of volumetric strain: (a) Relationship between volumetric strain and number of cycles N, (b) Relationship between volumetric strain and axial strain.

and redistribution of grain particles.

Fig. 8(b) illustrates the relationship between volumetric strain and axial strain, showing that as the number of loading cycles increases, both volumetric strain and axial strain gradually increase, exhibiting a “sparse to dense” pattern. However, as shown in Fig. 8(b), the magnitude of change in axial strain is generally greater than that in volumetric strain. Under the influence of confining pressure and initial deviatoric stress, the calcareous sand becomes compacted.

As discussed by Indraratna et al. [62,63], repeated loading and unloading of cyclic loads cause the calcareous sand particles to roll, rotate, and slide, leading to a rearrangement of their relative positions. Under cyclic loading, the long edges of calcareous sand particles tend to align perpendicular to the direction of the load, which is horizontal in this experiment. This alignment results in closer particle contact, leading to lateral expansion and axial compression. However, when the number of cycles loading increases to a certain extent, the distance between particles is reduced, and the interparticle pressure and frictional forces increase, causing the calcareous sand to become “harder” and less susceptible to particle sliding, thereby slowing the growth rate of both volumetric strain and axial strain.

3.4. Effects of confining pressure, initial deviatoric stress, and cyclic stress

The accumulated axial strain of calcareous sand is influenced by the combined effects of confining pressure, initial deviatoric stress, and cyclic stress. Fig. 9 illustrates the impact of these factors on the final accumulated axial strain of calcareous sand. The results show that an increase in confining pressure leads to a reduction in the final accumulated axial strain, demonstrating the restraining effect of confining pressure on the deformation of calcareous sand under cyclic loading.

For instance, under the conditions of $\eta_s = 0.4$ and $\eta_d = 0.6$, when the confining pressure $\sigma_c = 100$ kPa, 200 kPa, and 300 kPa, the cumulative axial strain of the sample at the 5000th cycle is 2.75 %, 2.5 %, and 1.92 %, respectively, with decay rates of 9.1 % and 23.2 %. Similar trends are observed under other values of initial deviatoric stress ratio (η_s). This phenomenon occurs primarily because, under the same deviatoric stress, lower confining pressure provides less constraint on the calcareous sand, allowing particles to move more freely and resulting in greater axial strain. This observation aligns with previous studies [29,64], which show that as confining pressure increases, the mean effective stress of the soil rises. This increase enhances particle interactions and the clamping force between them, thereby mitigating axial strain. The underlying mechanism is illustrated in Fig. 10(a).

In resisting the axial deformation of calcareous sand, initial deviatoric stress plays a significant role. The increase in interaction forces between soil particles is influenced by the rise in the soil’s effective mean stress [58]. Notably, an increase in the initial deviatoric stress also leads to a rise in the soil’s effective mean stress. As the initial deviatoric stress grows, the effective mean stress between calcareous sand particles increases, tightening their connections, particularly along the direction of the initial deviatoric stress, thereby enhancing their resistance to deformation, as illustrated in Fig. 10(b).

Fig. 9 also shows that as the cyclic stress ratio (η_d) increases, the cumulative axial strain exhibits an upward trend. Compared to the effects of confining pressure and initial deviatoric stress, has a more

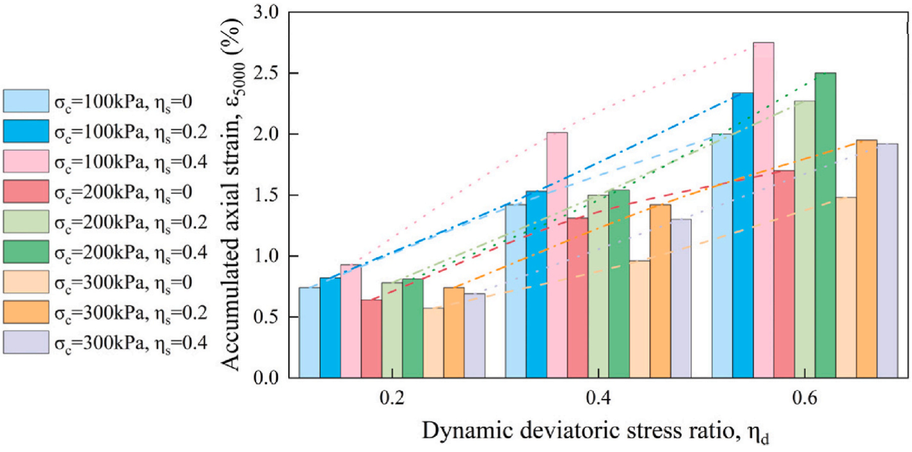

Fig. 9. Variation trend of axial strain in calcareous sand under different factors.

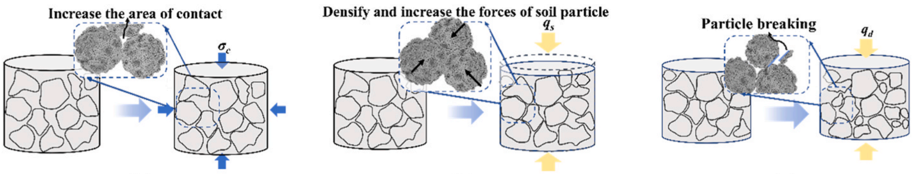

(a) (b) (c)

Fig. 10. Trend of calcareous sand failure: (a) Enhanced contact between particles (b) Increased interaction between particles (c) Particle breaking under load.

pronounced impact. For instance, when $\sigma_c = 300$ kPa and $\eta_s = 0.4$, the final cumulative axial strain of the sample is 0.69, 1.3, and 1.92 for η_d of 0.2, 0.4, and 0.6, respectively, corresponding to increase rates of 88.4 % and 89.56 %. This is primarily attributed to the increased movement of sand particles under cyclic loading, which leads to a more compact arrangement of calcareous sand structure [65].

However, the cumulative axial strain of calcareous sand is not solely attributed to particle rearrangement. Particle wear also plays a critical role by influencing the interlocking force within the particle chain [66, 67]. More specifically, under cyclic loading, the sharp edges and rough surfaces of the particles become smoother, while the fine particles generated by wear fill the voids within the sample. This process reduces the interlocking force between particles, as illustrated in Fig. 10(c). Consequently, the sample becomes more compact, and the effect becomes intensifies with increasing cyclic stress [28,68].

It is important to highlight that the initial deviatoric stress exhibits a “dual nature”: while it can increase the effective stress, enhancing the calcareous sand’s resistance to deformation, it can also interact with cyclic stress to cause particle wear and disrupt the force chain, leading to further compression of the soil. For instance, when $\sigma_c = 300$ kPa and $\eta_d = 0.6$, the cumulative axial strain of the sample at the 5000th cycle is 1.48 %, 1.95 %, and 1.92 % for initial deviatoric stress ratios (η_s) of 0.2, 0.4, and 0.6, respectively. This behavior is primarily due to the sliding force generated by the combined effects of cyclic stress and initial deviatoric stress, which exceeds the resistance provided by the interlocking force chain [69].

3.5. The stress paths

To further investigate the effects of confining pressure (σ_c), initial deviatoric stress ratio (η_s), and cyclic stress ratio (η_d) on the accumulated deformation of calcareous sand, this study employs the loading stress path (LSP), loading-residual stress path (LRSP), the linear distance from the end of the LSP to the critical state line, and their ratio LSP/LRSP for as analytical parameters.

The study evaluates the impacts of two consolidation modes: isotropic consolidation and deviatoric consolidation. The corresponding stress path diagrams are shown in Fig. 11, respectively. In these figures, the LSP and LRSP are defined by Eqs. (7) and (8), respectively.

$$LSP = \sigma_c + \sqrt{{q_s}^2 + (p_s - \sigma_c)^2} + \frac{\sqrt{10}}{3}\eta_d p_s \tag{7}$$

$$LRSP = \sqrt{(q_{CSL} - {q_s}^2)^2 + (p_{CSL} - p_s)^2} - \frac{\sqrt{10}}{3}\eta_d p_s \tag{8}$$

where p_{csl} and q_{csl} are the mean effective stress and deviatoric stress at critical state, respectively.

The relationship between ε_{100} and LSP is illustrated in Fig. 12. A linear positive correlation with LSP is observed, indicating that the cumulative axial strain generated by calcareous sand under cyclic loading conditions depends on initial consolidation and cyclic load parameters. The magnitude of LSP is directly influenced by factors such as confining pressure (σ_c), initial deviatoric stress ratio (η_s), and cyclic stress ratio (η_d), which subsequently affect the cumulative deformation characteristics of calcareous sand. It is also noteworthy that as the confining pressure increases from 100 kPa to 300 kPa, the ranges of both the 95 % confidence band and the 95 % prediction band narrow. This suggests that higher confining pressure results in a stronger positive correlation with LSP.

Fig. 13 illustrates the relationship between ε_{100} and the ratio of LSP/LRSP. The LSP/LRSP ratio represents the proximity of the current stress level of calcareous sand to the critical state line. A higher LSP/LRSP ratio indicates that the stress level is closer to the critical state line, suggesting that the soil is in a more unstable condition and has a higher potential for failure [14]. Specifically, under identical confining pressure conditions, an increase in both the cyclic stress ratio and the initial deviatoric stress results in a higher LSP/LRSP ratio. Conversely, a reduction in these parameters lowers the specimen’s resistance to deformation. This finding underscores that the cumulative volumetric deformation characteristics of calcareous sand are closely dependent on its.

Fig. 13 indicates that an increase in confining pressure raises in the upper limit value of LRSP, further confirming that specimens exhibit greater resistance to failure at a confining pressure of 300 kPa compared to lower pressures. This analysis also highlights three key factors influencing cumulative axial strain. Since the stress path is closely associated with the deformation behavior of calcareous sand, it is feasible to

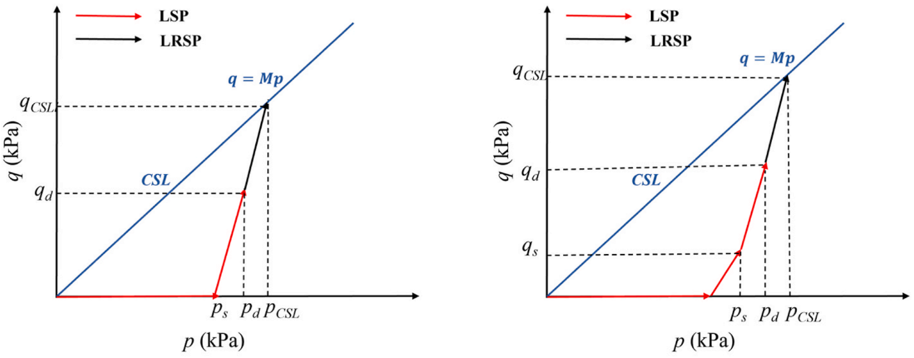

(a) (b)

Fig. 11. Schematic diagram of stress paths for (a) Isotropic consolidation stress path (b) Anisotropic consolidation following isotropic consolidation.

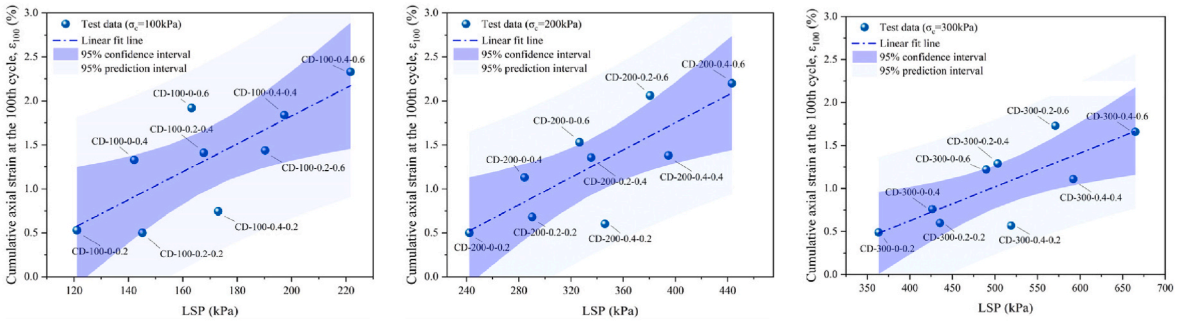

(a) (b) (c)

Fig. 12. Relationship between cumulative axial strain and LSP in 100th cycle: (a) $\sigma_c = 100$ kPa; (b) $\sigma_c = 200$ kPa; (c) $\sigma_c = 300$ kPa.

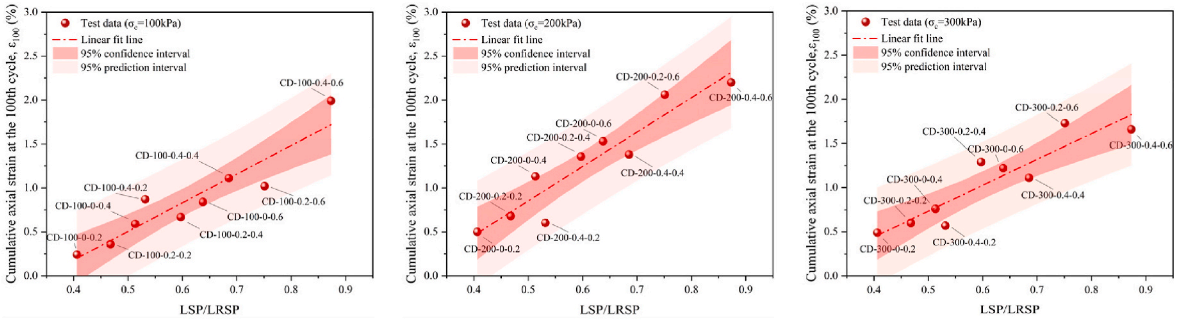

(a) (b) (c)

Fig. 13. Relationship between cumulative axial strain and LSP/LRSP in the 100th cycle: (a) $\sigma_c = 100$ kPa; (b) $\sigma_c = 200$ kPa; (c) $\sigma_c = 300$ kPa.

develop a model for cumulative axial strain based on the stress path.

4. Development of a prediction model

Creating a model to predict how calcareous sand deforms in marine construction is very useful, especially for building strong pile foundations and roadbeds. This model helps engineers better understand and reduce the risk of deformation, making marine structures safer and more stable. For example, single-pile wind power generation structures are exposed to both wind and wave loads, causing cumulative deformation. Additionally, the subgrade is impacted by traffic loads during operation, leading to settlement.

4.1. Model development

As previously mentioned, confining pressures (σ_c), initial deviatoric stress ratios (η_s), and cyclic stress ratios (η_d) collectively influence the cumulative axial strain of calcareous sand. Therefore, to ensure the safe design of marine infrastructure, this paper presents a predictive model for cumulative axial deformation that takes into account confining pressure (σ_c), initial deviatoric stress ratios (η_s), and cyclic stress ratios (η_d).

In the investigation of cumulative deformation under cyclic loading, Monismith et al. [38] proposed a representative model for cumulative plastic deformation:

$$A_0\varepsilon_p = N^b \tag{9}$$

where ε_p is cumulative plastic deformation, N is the number of cyclic loads, and A_0 and b are fitting parameters.

He et al. [41] conducted a triaxial test on calcareous sand samples collected from the South China Sea. They further refined the cumulative plastic deformation model in Eq. (9) by incorporating parameter A_0, and established a cumulative strain model specifically for calcareous sand. The proposed model demonstrates a strong fitting performance, and the corresponding formula is as follows:

$$\lg\left(\frac{\varepsilon_N}{\varepsilon_1}\right) = B \lg N \tag{10}$$

where ε_N is the cumulative axial strain of the N-th cycle, ε_1 is the cumulative axial strain of the initial cycle, N is the total number of cycles, and B is defined as the fitting coefficient. According to the experimental results, it can be observed that the axial strain of calcareous sand is most unstable during the first cycle of loading. This instability primarily arises from the instantaneous deformation induced by applied loads under drained conditions. Furthermore, due to variations in pore water pressure, subsequent cycles exhibit instability and do not adequately reflect the initial state. Therefore, this study utilizes the cumulative axial strain from the first 100 cycles to characterize the effects of initial consolidation state and cyclic stress. Specifically, the cumulative axial strain ε_1 from the first cycle in Eq. (10) is adjusted to reflect the cumulative axial strain ε_{100} from the 100th cycle. The modified expression is presented as Eq. (11).

$$\lg\left(\frac{\varepsilon_N}{\varepsilon_{100}}\right) = B \lg N \tag{11}$$

in this state, the behavior of the specimen is primarily influenced by three factors: initial deviatoric stress q_s, cyclic stress q_d, and initial mean principal stress p_s. Therefore, the accumulated axial strain after the 100th cycle can be expressed as Eq. (12).

$$\varepsilon_{100} = F(q_s, q_d, p_s) \tag{12}$$

To investigate the effect of p_s on cumulative axial strain, the initial average principal stress was normalized, and $\frac{p_s}{p_a}$ was used for the study. The constraint behavior of $\frac{p_s}{p_a}$ in the experiments was characterized by the function G (p_s), as described in Eq. (13).

$$G(p_s)=\frac{\lg\left(A\frac{p_s}{p_a}+1\right)}{A\frac{p_s}{p_a}+1} \tag{13}$$

By combining Eqs. (12) and (13), the functional expression of the function can be represented as Eq. (14).

$$\varepsilon_{100}=F(q_s,q_d)\frac{\lg\left(A\frac{p_s}{p_a}+1\right)}{A\frac{p_s}{p_a}+1} \tag{14}$$

where F (q_s, q_d) is a hidden function linked to initial deviatoric stress q_s and cyclic stress q_d. A denotes the influence factor of the initial average principal stress. To explore the relationship between the F (q_s, q_d) and the q_s and q_d, Huang and Yao [70] employed the relative residual stress level to examine the effect of residual stress on cumulative strain. Their analysis results aligned with actual observations. The specific expression of the relative residual stress is presented in Eq. (15).

$$D^*=\frac{D_p-D_s}{D_{\max}-D_s} \tag{15}$$

Where $D_{\max}$ is the maximum achievable level of residual stress, which is set to 1. $D_s=\frac{q_s}{q_{cri}}$ is the initial deviatoric stress level, $D_s^1=\frac{q_d}{q_{cri}}$ is the cyclic stress level during the loading cycle, and q_{cri} signifies the peak residual stress. This study redefines the calculation process for the cyclic stress level based on the peak residual stress calculation method for the stress path plane along the critical state line. The formula for the cyclic stress level is provided in Eq. (16):

$$D_p=\frac{q_s+q_d}{q_{cri}} \tag{16}$$

where q_{cri} is represented in the q-p plane as the vertical coordinate of the intersection point between the stress path during loading and the LRSP, as illustrated in Fig. 14.

According to Fig. 14, the deviatoric stress and peak deviatoric stress are expressed by Eqs. (17) and (18), respectively:

$$q=3(p-p_s)+q_s \tag{17}$$

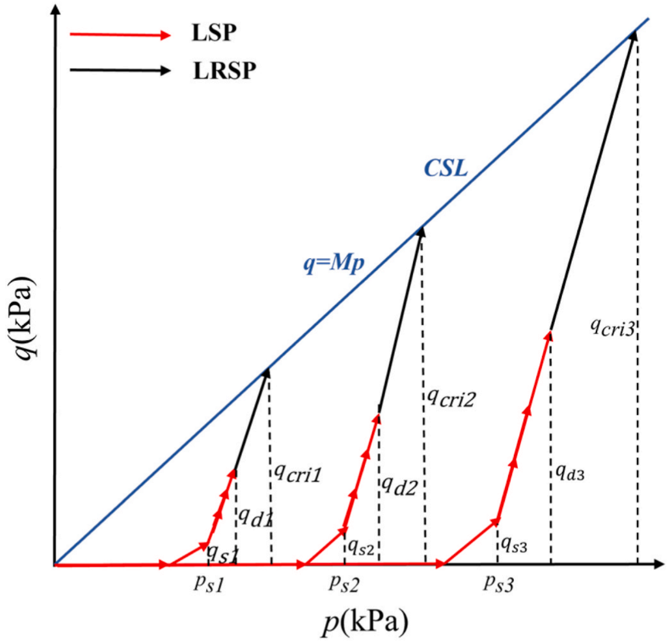

Fig. 14. Schematic diagram of deviatoric stress level parameters.

$$q_{cri}=(3p_s-q_s)\frac{M}{3-M} \tag{18}$$

From Eqs. 15–18, the initial deviatoric stress level D_S, cyclic stress level D_p, and relative residual stress level D^* can be derived in relation to the initial average principal stress q_s, initial static residual stress p_s, and cyclic stress p_d, as presented in Eqs. 19–21:

$$D_s=\frac{(3-M)p_s}{M(3q_s-p_s)} \tag{19}$$

$$D_p=\frac{(3-M)(q_s+q_d)}{M(3p_s-q_s)} \tag{20}$$

$$D^*=\frac{(3-M)q_d}{3(Mp_s-q_s)} \tag{21}$$

The relative deviatoric stress level parameter represents the current dynamic deviatoric stress level of the soil. The cyclic stress level D_p and the relative deviatoric stress level D^* were utilized to categorize the experimental data. Fig. 15 presents the progression of the cumulative axial strain ε_{100} concerning the cyclic stress level D_p and the relative deviatoric stress level D^* for the 100th loading cycle.

Fig. 15 demonstrates that the relative residual stress level D^* exhibits a stronger linear correlation with the cumulative axial strain ε_{100} at the 100th cycle than with the cyclic stress level D_p. Since D^* accounts for the combined effects of the initial static residual stress D_s and the cyclic stress D_p, it provides a more precise characterization of their influence. Therefore, in the following formula derivation, D^* is employed to represent the effect of residual stress in the subsequent formula derivation.

To explore the mathematical relationship between the relative deviatoric stress level D^* and the cumulative axial strain ε_{100} after the 100th cycle, G (p_s) and ε_{100} were normalized to remove the influence of the initial average principal stress p_s on ε_{100}, thereby deriving the discrete values of F (q_s, q_d). Fig. 16 presents a relationship diagram between D^* and F (q_s, q_d), constructed using the experimental data. The strong linear relationship between them is evident, and it is mathematically represented by Eq. (22):

$$F(q_s,q_d)=CD \tag{22}$$

where D is the relative deviatoric stress level, and C is the influence factor of D.

Using Eqs. (14), (21) and (22), the cumulative deformation of calcareous sand is derived and expressed as Eq. (23):

$$\varepsilon_N=C\frac{(3-M)q_d}{3(Mp_s-q_s)}\frac{\lg\left(A\frac{p_s}{p_a}+1\right)}{A\frac{p_s}{p_a}+1}N^B \tag{23}$$

where, ε_N is the cumulative axial strain at the N-th cycle; p_s is the initial average principal stress; p_a is 1 atm, defined as 101 kPa; N is the number of cycles loading; B is the influence factor associated with N; A is the influence factor of p_s; D is the relative deviatoric stress level; C is the influence factor of D; and M is the slope of the CSL (critical state line) for calcareous sand. The parameters A, B, C, and M are determined using the following method:

(1) The parameter A (the influence factor of p_s)

To investigate the effect of initial average principal stress on the cumulative axial strain of calcareous sand, the influence of initial deviatoric stress is excluded. Specifically, experimental data under the condition $\eta_s=0$ are used. Eq. (14) is employed to generate Fig. 17, and the average value of A is calculated as 2.2507.

(2) The parameter B (the influence factor associated with N)

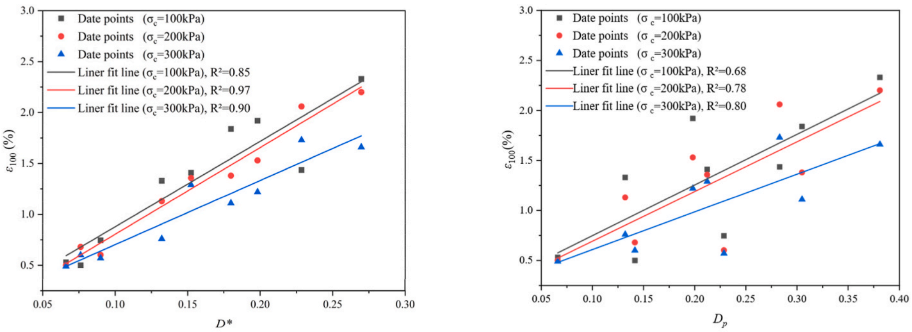

(a) (b)

Fig. 15. Relationship between ε and relative deviatoric stress level D^* and dynamic stress level D_p, (a) Relative deviatoric stress level D^*, (b) Dynamic stress level D_p.

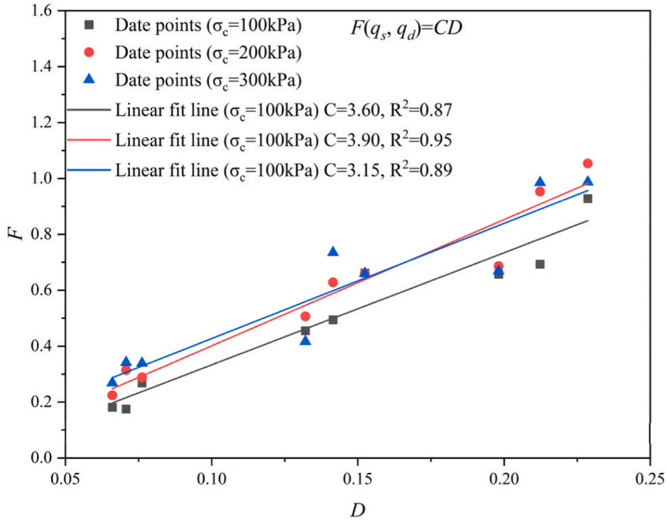

Fig. 16. Relationship between F (q_s, q_d) and deviatoric stress level D.

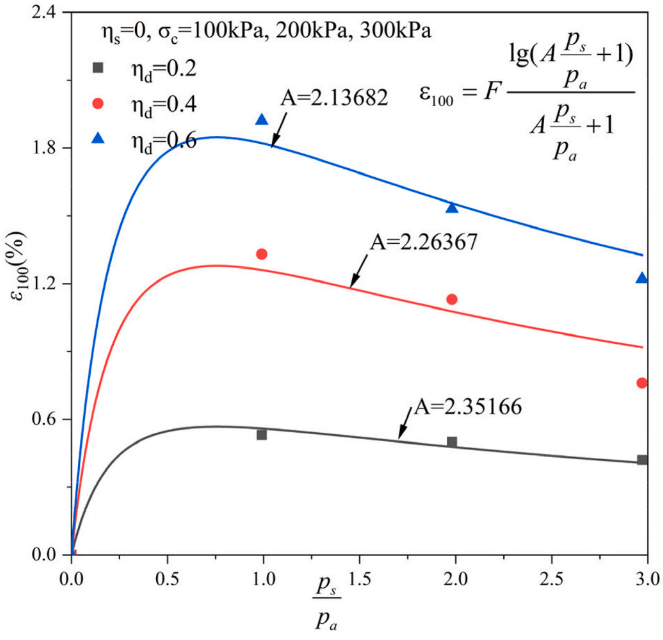

Fig. 17. The relationship between ε_{100} and p_s/p_a.

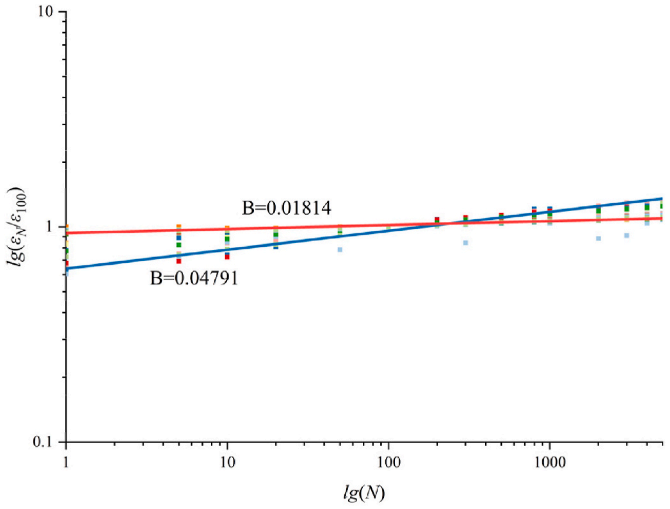

Fig. 18. The relationship between $\varepsilon_N/\varepsilon_{100}$ and N.

The relationship curve between $\varepsilon_N/\varepsilon_{100}$ and N is presented in Fig. 18. The double logarithmic plot exhibits strong linearity, with the slope B of the relationship ranging from 0.01814 to 0.04791. This indicates minimal variation across multiple sets of experimental datasets, with the average slope calculated as $B = 0.038004$.

(3) The parameters C (the influence factor of D) and M (the slope of the critical state line)

The parameter C can be derived from Fig. 16, with an average value of 23.4. For the value of M, it was determined through prior triaxial shear tests on calcareous sand with a relative density of 50 % and the M of its CSL is 1.50.

In summary, the four parameters of the model are outlined as Table 4:

4.2. Model effectiveness and accuracy

To evaluate the effectiveness and accuracy of the developed model for evaluating the cumulative deformation of saturated calcareous sand

Table 4
Model parameters.

Parameters	Value
A	2.2507
B	0.038004
C	23.4
M	1.50

under cyclic loading, the model was validated using Eq. (23). Two distinct validation tests were conducted to assess the predictive capacity and applicability of the proposed constitutive model.

4.2.1. Model verification with original data

In this comparison study, both the theoretical and predicted results for the cyclic cumulative deformation of saturated calcareous sand are shown in Fig. 19. As shown, the theoretical values closely match the experimental data, demonstrating excellent agreement. This outcome confirms the reliability of the cyclic cumulative deformation calculation model for saturated calcareous sand, emphasizing its ability to accurately represent the deformation characteristics of the soil under cyclic loading conditions.

4.2.2. Cross-validation with literature data

To further verify the applicability of the model, the model (Eq. (23)) proposed in this study was compared with the Model 6 of Table 1 presented by He et al. [41] and Model 8 of Table 1, the High-Cycle Accumulation (HCA) improved by Wichtmann et al. [51]. The study concentrates on the coupled effects of confining pressure (σ_c), initial deviatoric stress (η_s), and cyclic stress (η_d). He's model, which addresses similar governing factors, and the HCA model developed by Niemunis and Wichtmann [48], known for its representativeness in describing strain accumulation in soils under cyclic loading, were selected for comparison with the experimental results obtained in this study. This comparison aims to assess the accuracy of the proposed model.

The verification data were obtained from triaxial experiments on calcareous sand conducted by Wang et al. [52]. The calcareous sand used in Wang's experiments was sourced from a reef in the South China Sea, with a relative density of 95 %. The tested samples exhibited a specific gravity of 2.75, a maximum void ratio of 1.27, and a minimum void ratio of 0.66. Table 5 summarizes the experimental scheme reported by Wang, where the loading frequency was kept at 1 Hz during the tests.

Fig. 20 compares the prediction results of the proposed model of Model 5 and 8. As illustrated in Fig. 20, the prediction results from the model proposed in this paper better fit the experimental results of Wang et al. [52]. The comparison also shows that the proposed model Eq. (23) achieves higher accuracy under lower cyclic stress ratios than under higher ones. In contrast, He's model consistently underestimates cumulative axial strain. Although Wichtmann's model delivers reasonable overall predictions, its performance during early-stage loading is markedly inferior to that of the proposed model.

In summary, the model developed in this study calculates cumulative strain in calcareous sand based on simple laboratory triaxial tests, considering the effects of confining pressure, deviatoric stress, and cyclic stress. The model incorporates the concept of the Critical State Line (CSL) from classical plasticity theory and is based on test results, leading to relatively concise formulations with fewer parameters, all of which can be obtained through conventional triaxial experiments.

5. Discussion and limitations

The model in this study is concise and straightforward. Nevertheless, this streamlined approach omits consideration of certain critical factors, notably particle breakage and the influence of particle shape. Calcareous sand exhibits notably different cumulative strain behaviors under varying stress conditions. Under high-stress conditions, particle breakage constitutes one of the primary mechanisms driving deformation. However, experimental observations within this study's medium-to-low confining pressure range (100–300 kPa) reveal measurable particle crushing in calcareous sand, with the degree of fragmentation varying according to stress conditions.

Fig. 21 presents the grain size distribution curves of soil samples following triaxial compression under varying confining pressures. These curves clearly demonstrate the influence of stress conditions on particle

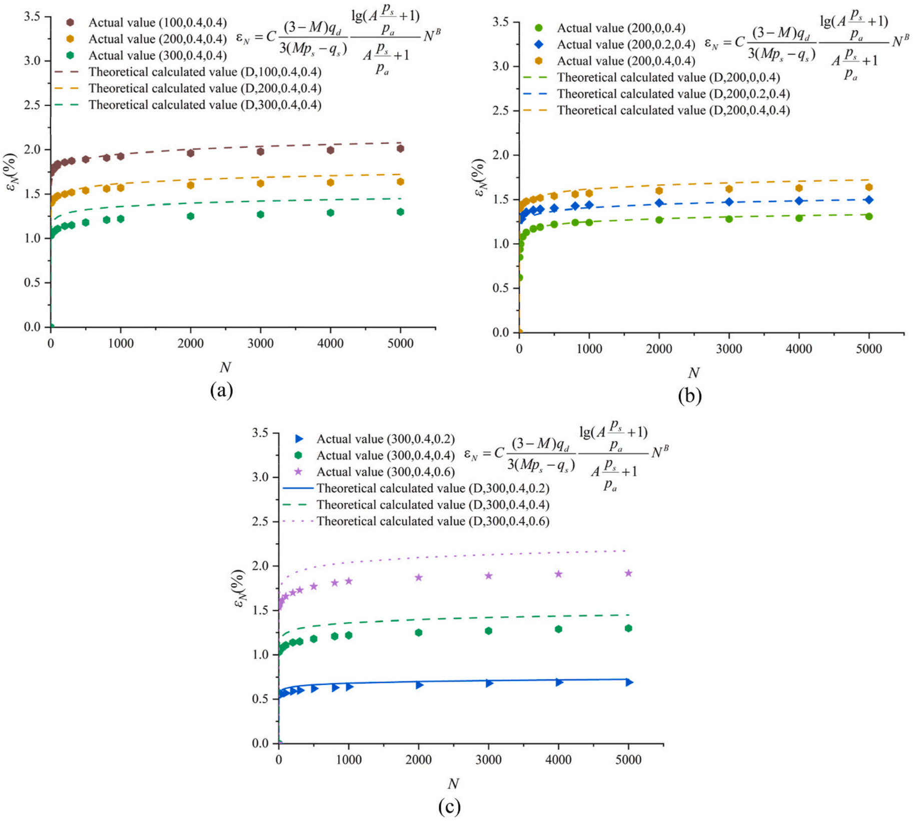

(a) (b) (c)

Fig. 19. Model calculation verification (a) Confining pressure (b) Initial deviatoric stress (c) Cyclic stress.

Table 5
The cyclic triaxial test conditions of Wang.

No.	Original Data			Required Data for Validation						
	σ_3	q_d	K_c	σ_c (kPa)	η_s	σ_{1c} (kPa)	p_s (kPa)	q_s (kPa)	η_d	q_d (kPa)
W-1	100	100	1.5	100	0.375	150	133.33	50	0.750	100
W-2	100	50	1.5	100	0.375	150	133.33	50	0.375	50
W-3	100	150	1.5	100	0.375	150	133.33	50	1.125	150
W-4	100	100	2.0	100	0.600	200	166.67	100	0.600	100

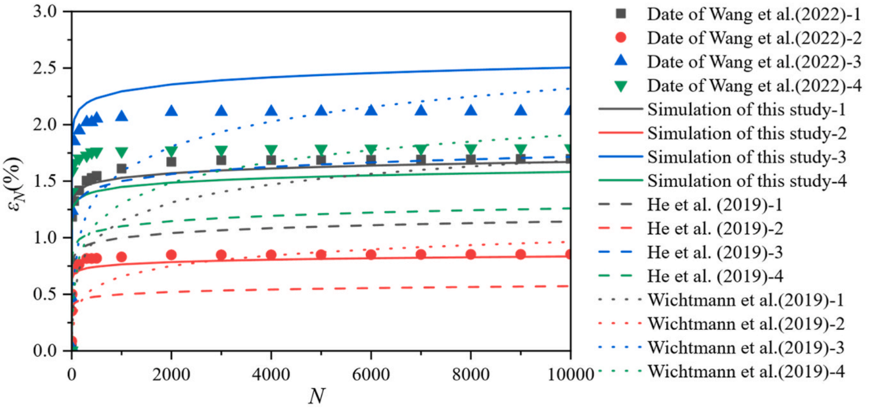

Note: (a) Simualtion of this is the Eq.(23); (b) He et al.(2019) is the Model 6 of Table 1; (c) Wichtmann et al.(2019) is the Model 8 of Table 1.

Fig. 20. Comparative validation of predictive model and existing models using experimental data of Wang et al.

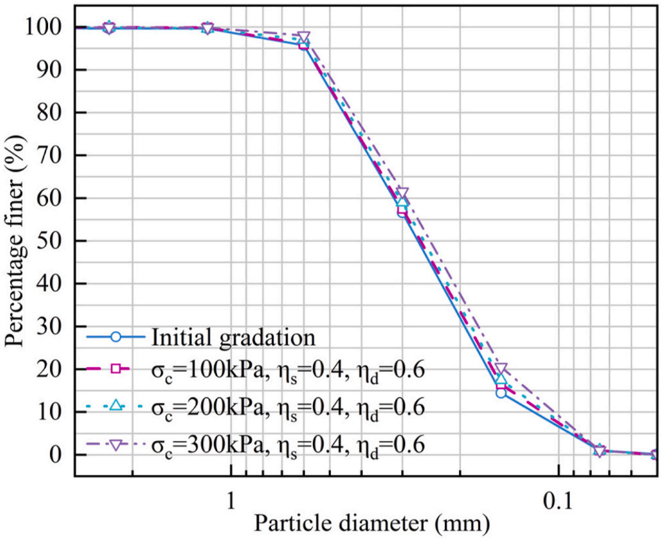

Fig. 21. Grain size distribution curves of dense samples after triaxial compression.

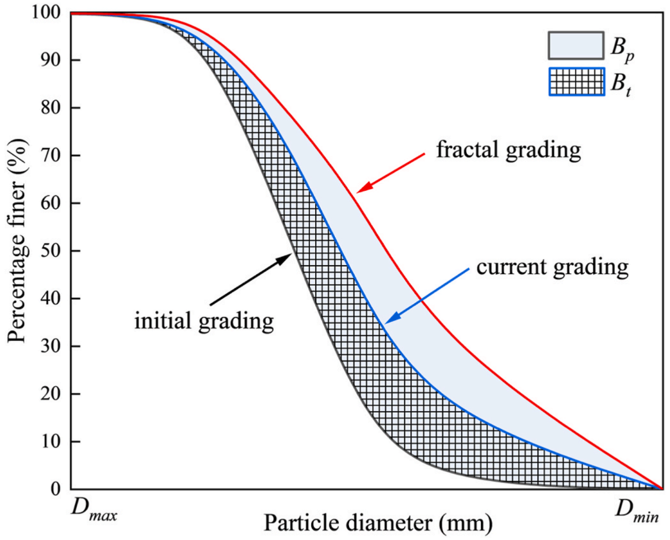

Fig. 22. Definition of relative breakage index.

breakage within the specimens. The observed variations in gradation characteristics provide insights into the mechanical behavior of the calcareous sand under different stress states.

The relative breakage index (B_r), originally proposed by Hardin [71], has become a fundamental metric for quantifying particle breakage in calcareous sands. Recent advancements by Einav [72] have redefined this relative breakage index using continuum mechanics principles, concurrently establishing a computational framework for breakage potential (B_p) by integrating fractal theory. This study employs the modified particle breakage index B_r proposed by Einav to quantify the extent of particle crushing. The schematic diagram of B_r calculation is presented in Fig. 22, where the hatched area represents the total breakage quantity (B_t), and the blue-shaded region corresponds to the breakage potential (B_p). The particle breakage index is defined as B_r=B_t/B_p.

Fig. 23 demonstrates the evolution of B_r with η_d under varying σ_c and η_s conditions. As illustrated, increasing η_d significantly enhances particle breakage development. For instance, under $\eta_s = 0$ and $\sigma_c = 300$ kPa, the test group with $\eta_d = 0.2$ exhibits a relative breakage ratio (B_r) of 1.25 %. When η_d increases to 0.4 and 0.6, B_r escalates to 2.25 % and 3.82 %, respectively. Zhang et al. [69]. demonstrated that intensified cyclic stress promotes particle breakage development using discrete element method studies. Notably, calcareous sand exhibits more pronounced breakage behavior compared to siliceous sand due to its metastable skeletal structure characterized by high intra-particle porosity and fragile biocementation.

Particle breakage under σ_c and η_s is fundamentally governed by effective stress mechanisms [73]. Notably, the η_s exhibits a pronounced

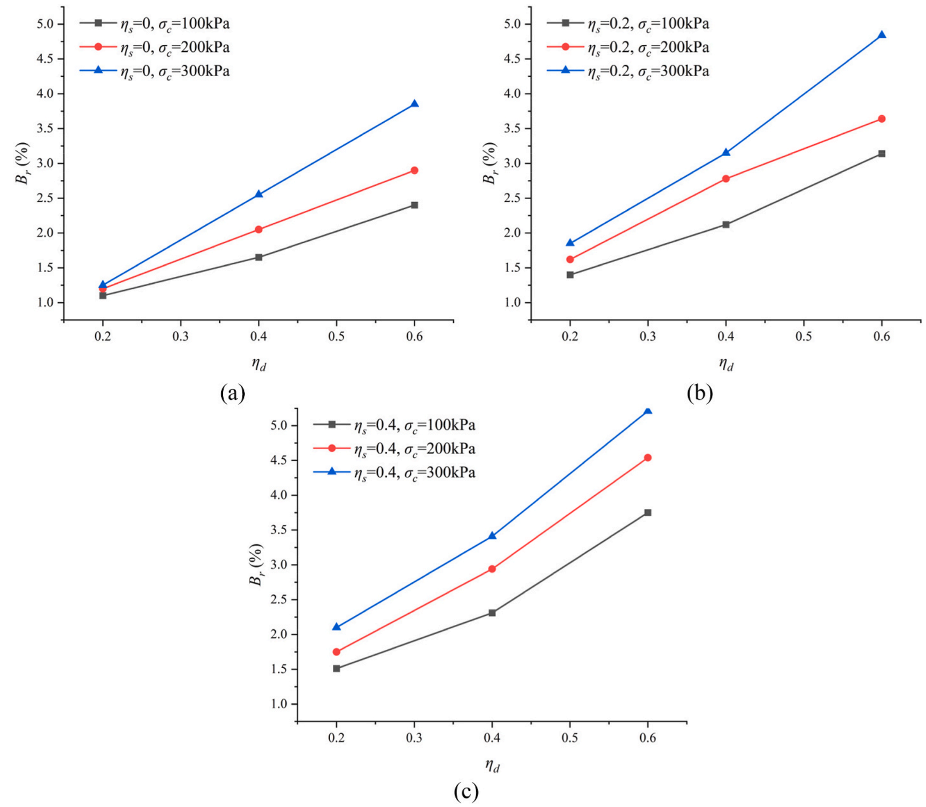

Fig. 23. Evolution of the relative breakage B_r with the η_d value considering σ_c and η_s, (a) $\eta_s = 0$, (b) $\eta_s = 0.2$, (c) $\eta_s = 0.4$.

catalytic effect on breakage evolution. With the increase of η_s, the particle breakage caused by d is more significant. For instance, under $\sigma_c = 100$ kPa with $\eta_s = 0$, increasing η_d from 0.2 to 0.6 elevates B_r by 50 % and 45.5 %, respectively. Contrastingly, under $\sigma_c = 100$ kPa with $\eta_s = 0.4$, the same η_d -increment drives B_r increases of 53 % and 62.3 %, respectively. This η_s and η_d synergy accentuates particle breakage progression, aligning with the previously proposed "dual nature" of η_s in simultaneously promoting cumulative strain.

Fig. 21 and the preceding analysis demonstrate measurable particle breakage in calcareous sand under medium-to-low confining pressures, but this mechanism remains unaccounted for in the proposed model in this study. Furthermore, particle morphology significantly influences cumulative deformation in practical engineering applications. The heightened inter-particle friction and interlocking provided by angular grains markedly intensify strain accumulation.

In addition, both fines content and relative density influence the accumulative strain of particulate materials under cyclic loading. Variations in the fines content alter interparticle stress distribution, leading to differential accumulation of strain. Higher relative density generally indicates a more compact soil structure, thereby reducing deformation.

Based on the discussion above, the main limitations and their possible improvements of this article are as follows.

(a) Lack of consideration of particle breakage. Although some parameters in the model consider the subtle effects of particle breakage during the fitting process, there is no in-depth fitting of the influence of particle breakage. Future models should integrate a detailed analysis of particle breakage mechanisms to enhance the accuracy of soil behavior predictions. Particular attention should be paid to the dynamic variations in particle breakage of calcareous sands under cyclic loading.
(b) Absence of the role of grain shape. The model does not quantify the influence of different grain shapes on deformation under load. Future research can analyze the specific impacts of particle shape on the mechanical response of calcareous sands and quantify their effects.
(c) Lack of assessment of fines content and relative density considerations. The relationship between fines content, relative density, and accumulated strain should be emphasized, especially focus on the influence of fine particle content and relative density on stress distribution under cyclic loading.

It is important to note that this study primarily focused on stress effects, with simplified assumptions regarding other factors, constituting a limitation of the current experimental setup.

Subsequent studies should focus on the coupled effects of particle breakage, grain shape, fines content, and relative density, with particular attention to the changes of particle breakage during the loading process. Emphasizing on their synergistic influences under marine environmental conditions.

6. Conclusions

This study investigated the cumulative deformation behavior of calcareous sand under cyclic loading conditions, offering valuable insights and practical applications for marine infrastructure and road foundation design. The following conclusions can be drawn based on the current study.

(1) The experimental results showed that cumulative axial strain in calcareous sand increases with the number of loading cycles; but, the rate of strain accumulation progressively diminishes. After approximately 100 cycles, the material transitions to a plastic stabilization phase, with minimal additional deformation observed in subsequent cycles.
(2) The cumulative deformation of calcareous sand is significantly influenced by confining pressure, initial deviatoric stress, and cyclic stress. Confining pressure effectively suppresses

cumulative axial strain, while cyclic stress promotes densification and particle fragmentation, exhibiting a strong correlation with cumulative strain. Initial static deviatoric stress enhances resistance to particle deformation through increased effective stress, but once the cyclic stress surpasses the interlocking force limit, it further promotes densification of the calcareous sand.

(3) Among the influencing factors, cyclic stress, and confining pressure play more dominant roles in driving cumulative deformation compared to initial static deviatoric stress. The cyclic stress ratio is the primary factor driving the stress path toward the CSL, with the initial deviatoric stress ratio (η_s) acting as a facilitator of this progression.

(4) An increase in η_d significantly enhances particle breakage (B_r) in calcareous sand, particularly under conditions of higher η_s and σ_c. Moreover, the synergy between η_s and η_d, governed by effective stress, accelerates particle breakage (B_r) in calcareous sand.

(5) A model was developed based on experimental data to predict the cyclic cumulative deformation of saturated calcareous sand. The model effectively incorporates the effects of confining pressure, cyclic stress, and initial static deviatoric stress, yielding predictions that closely match experimental observations. This confirms the model's reliability and practical applicability.

The finding of this study deepens the understanding of cumulative deformation calcareous sand subjected to wave-induced cyclic loads. The proposed model provides a robust tool for predicting soil deformation, aiding engineers in designing and optimizing marine and road foundations. Furthermore, the study highlights the potential for utilizing calcareous sand in sustainable infrastructure projects, ensuring safety, reliability, and long-term performance in challenging marine environments. Given that calcareous sand exhibits pronounced stress-dependent behavior and relatively weak particle structures, incorporating particle breakage, grain shape, fines content, and high confining pressure would significantly enhance the understanding of cumulative strain evolution. Future investigations should focus on these critical aspects to advance the mechanistic interpretation of the cyclic deformation behavior of calcareous sand.

CRediT authorship contribution statement

Bingxiang Yuan: Supervision, Project administration, Methodology. **Xianlun Huang:** Writing – original draft, Visualization, Software, Investigation, Conceptualization. **Runcheng Li:** Visualization, Software, Investigation. **Qingzi Luo:** Validation, Software, Formal analysis. **Jim Shiau:** Writing – review & editing, Investigation, Formal analysis. **Yonghong Wang:** Visualization, Investigation, Formal analysis. **Junhong Yuan:** Writing – review & editing, Visualization, Software. **Sabri Mohanad Muayad Sabri:** Writing – review & editing, Visualization, Investigation. **Shiyuan Huang:** Investigation, Formal analysis. **Cheng Liao:** Investigation, Formal analysis.

Declaration of competing interest

The authors declare the following financial interests/personal relationships which may be considered as potential competing interests: Bingxiang Yuan reports financial support was provided by National Natural Science Foundations of China. Bingxiang Yuan reports financial support was provided by Guangdong Basic and Applied Research Foundations. Xianlun Huang reports equipment, drugs, or supplies was provided by Shiyanjia Lab. If there are other authors, they declare that they have no known competing financial interests or personal relationships that could have appeared to influence the work reported in this paper.

Acknowledgements

The authors would like to acknowledge the support provided by the National Natural Science Foundations of China (No. 52278336 and 51978177), Guangdong Basic and Applied Research Foundations (No. 2023B1515020061 and 2022A1515240037). The help from Shiyanjia Lab (http://www.shiyanjia.com) in performing SEM experiments is greatly appreciated. And we also appreciate the paper polishing from the Prof. Jim Shaiau, University of Southern Queensland in Australia.

Data availability

Data will be made available on request.

References

[1] Gao Y, Shi T, Yuan Q, Sun K. The creep characteristics and related evolution of particle morphology for calcareous sand. Powder Technol 2024;431:119077. https://doi.org/10.1016/j.powtec.2023.119077.

[2] Hu H, Luo L, Lei G, Guo J, He S, Hu X, et al. The transverse bearing characteristics of the pile foundation in a calcareous sand area. Materials 2022;15:6176. https://doi.org/10.3390/ma15176176.

[3] Pei H, Wang D, Liu Q. Numerical study of relationships between the cone resistances and footing bearing capacities in silica and calcareous sands. Comput Geotech 2023;155:105220. https://doi.org/10.1016/j.compgeo.2022.105220.

[4] Wei H, Liu H, Li X, Tao Z, Wu Y, Shen J, et al. Effect of stress path on the mechanical properties of calcareous sand. Undergr Space 2023;9:20–30. https://doi.org/10.1016/j.undsp.2022.06.003.

[5] Coop MR, Sorensen KK, Bodas Freitas T, Georgoutsos G. Particle breakage during shearing of a carbonate sand. Geotechnique 2004;54:157–63. https://doi.org/10.1680/geot.2004.54.3.157.

[6] Ding Z, He S-H, Sun Y, Xia T-D, Zhang Q-F. Comparative study on cyclic behavior of marine calcareous sand and terrigenous siliceous sand for transportation infrastructure applications. Constr Build Mater 2021;283:122740. https://doi.org/10.1016/j.conbuildmat.2021.122740.

[7] Wu Y, Yamamoto H, Cui J, Cheng H. Influence of load mode on particle crushing characteristics of silica sand at high stresses. Int J GeoMech 2020;20:04019194. https://doi.org/10.1061/(ASCE)GM.1943-5622.0001600.

[8] Yuan B, Fan L, Li Z, Luo Q, Wang Y, Xing H, et al. Experimental study on pile-soil interaction under horizontal load in layered foundation. China J Highw Transp 2022;35:62–72. https://doi.org/10.19721/j.cnki.1001-7372.2022.11.007 (in English).

[9] Yu J, Lu C, Leung CKY, Li G. Mechanical properties of green structural concrete with ultrahigh-volume fly ash. Constr Build Mater 2017;147:510–8. https://doi.org/10.1016/j.conbuildmat.2017.04.188.

[10] Yuan B, Chen M, Chen W, Luo Q, Li H. Effect of pile-soil relative stiffness on deformation characteristics of the laterally loaded pile. Adv Mater Sci Eng 2022; 2022:1–13. https://doi.org/10.1155/2022/4913887.

[11] Yuan B, Li Z, Zhao Z, Ni H, Su Z, Li Z. Experimental study of displacement field of layered soils surrounding laterally loaded pile based on transparent soil. J Soils Sediments 2021;21:3072–83. https://doi.org/10.1007/s11368-021-03004-y.

[12] Liu L, Yao X, Ji Z, Gao H, Wang Z, Shen Z. Cyclic behavior of calcareous sand from the South China Sea. J Mar Sci Eng 2021;9:1014. https://doi.org/10.3390/jmse9091014.

[13] Karg C, Haegeman W. Elasto-plastic long-term behavior of granular soils: experimental investigation. Soil Dynam Earthq Eng 2009;29:155–72. https://doi.org/10.1016/j.soildyn.2008.01.001.

[14] He S, Ding Z, Xia T, Zhou W, Gan X, Chen Y, et al. Long-term behaviour and degradation of calcareous sand under cyclic loading. Eng Geol 2020;276:105756. https://doi.org/10.1016/j.enggeo.2020.105756.

[15] Lu D, Meng F, Zhou X, Zhuo Y, Gao Z, Du X. A dynamic elastoplastic model of concrete based on a modeling method with environmental factors as constitutive variables. J Eng Mech 2023;149:04023102. https://doi.org/10.1061/JENMDT.EMENG-7206.

[16] Lu D, Wang G, Du X, Wang Y. A nonlinear dynamic uniaxial strength criterion that considers the ultimate dynamic strength of concrete. Int J Impact Eng 2017;103:124–37. https://doi.org/10.1016/j.ijimpeng.2017.01.011.

[17] Yang B, Chen Y, Zhao C, Li Z. Effect of geotextiles with different masses per unit area on water loss and cracking under bottom water loss soil conditions. Geotext Geomembranes 2024;52:233–40. https://doi.org/10.1016/j.geotexmem.2023.10.006.

[18] Salem M, Elmamlouk H, Agaiby S. Static and cyclic behavior of north Coast calcareous sand in Egypt. Soil Dynam Earthq Eng 2013;55:83–91. https://doi.org/10.1016/j.soildyn.2013.09.001.

[19] Wei H, Zhao T, He J, Meng Q, Wang X. Evolution of particle breakage for calcareous sands during ring shear tests. Int J GeoMech 2018;18:04017153. https://doi.org/10.1061/(ASCE)GM.1943-5622.0001073.

[20] Yuan B, Liang J, Zhang B, Chen W, Huang X, Huang Q, et al. Optimized reinforcement of granite residual soil using a cement and alkaline solution: a coupling effect. J Rock Mech Geotech Eng 2024. https://doi.org/10.1016/j.jrmge.2024.01.009.

[21] Meng K, Cui C, Liang Z, Li H, Pei H. A new approach for longitudinal vibration of a large-diameter floating pipe pile in visco-elastic soil considering the three-dimensional wave effects. Comput Geotech 2020;128:103840. https://doi.org/10.1016/j.compgeo.2020.103840.

[22] Qadimi A, Coop MR. The undrained cyclic behaviour of a carbonate sand. Geotechnique 2007;57:739–50. https://doi.org/10.1680/geot.2007.57.9.739.

[23] Suescun-Florez E, Iskander M. Effect of fast constant loading rates on the global behavior of sand in triaxial compression. Geotech Test J 2017;40:52–71. https://doi.org/10.1520/GTJ20150253.

[24] Yuan B, Liang J, Huang X, Huang Q, Zhang B, Yang G, et al. Eco-efficient recycling of engineering muck for manufacturing low-carbon geopolymers assessed through LCA: exploring the impact of synthesis conditions on performance. Acta Geotech 2024. https://doi.org/10.1007/s11440-024-02395-9.

[25] Lv Y, Liu J, Xiong Z. One-dimensional dynamic compressive behavior of dry calcareous sand at high strain rates. J Rock Mech Geotech Eng 2019;11:192–201. https://doi.org/10.1016/j.jrmge.2018.04.013.

[26] Saeidaskari J, Alibolandi M, Azizkandi AS. Undrained monotonic and cyclic behavior of Qeshm calcareous sand. Mar Georesour Geotechnol 2021;39:798–811. https://doi.org/10.1080/1064119X.2020.1764678.

[27] Zhang Y, Liu X, Wang C, Zhang Z, Jiang S, Ma Z. Development of sustainable geopolymer with excavation soil powder as precursor: cementitious properties and thermal-activated modification. J Build Eng 2024;91:109745. https://doi.org/10.1016/j.jobe.2024.109745.

[28] Sun QD, Indraratna B, Nimbalkar S. Deformation and degradation mechanisms of railway ballast under high frequency cyclic loading. J Geotech Geoenviron Eng 2016;142:04015056. https://doi.org/10.1061/(ASCE)GT.1943-5606.0001375.

[29] He S, Ding Z, Goudarzy M, Sun Y, Yin Z-Y. Effect of variable confining pressure on the long-term cyclic behaviour of calcareous sand: experimental observation and microstructural interpretation. Can Geotech J 2023. https://doi.org/10.1139/cgj-2022-0492.

[30] Wang K, Chen Z, Wang Z, Chen Q, Ma D. Critical dynamic stress and cumulative plastic deformation of calcareous sand filler based on shakedown theory. J Mar Sci Eng 2023;11:195. https://doi.org/10.3390/jmse11010195.

[31] Qian H, Wu W, Xu C, Liao D, Du X. An extended hypoplastic constitutive model considering particle breakage for granular material. Comput Geotech 2023;159:105503. https://doi.org/10.1016/j.compgeo.2023.105503.

[32] Wang G, Wang Z, Ye Q, Zha J. Particle breakage evolution of coral sand using triaxial compression tests. J Rock Mech Geotech Eng 2021;13:321–34. https://doi.org/10.1016/j.jrmge.2020.06.010.

[33] Wu Y, Li N, Wang X, Cui J, Chen Y, Wu Y, et al. Experimental investigation on mechanical behavior and particle crushing of calcareous sand retrieved from South China Sea. Eng Geol 2021;280:105932. https://doi.org/10.1016/j.enggeo.2020.105932.

[34] Altuhafi FN, Coop MR. Changes to particle characteristics associated with the compression of sands. Geotechnique 2011;61:459–71. https://doi.org/10.1680/geot.9. 114.

[35] Kou H, Diao W, Zhang W, Zheng J, Ni P, Jang B-A, et al. Experimental study of interface shearing between calcareous sand and steel plate considering surface roughness and particle size. Appl Ocean Res 2021;107:102490. https://doi.org/10.1016/j.apor.2020.102490.

[36] Gao R, Ye J. A novel relationship between elastic modulus and void ratio associated with principal stress for coral calcareous sand. J Rock Mech Geotech Eng 2024;16:1033–48. https://doi.org/10.1016/j.jrmge.2023.07.011.

[37] Bai B, Zhou R, Cai G, Hu W, Yang G. Coupled thermo-hydro-mechanical mechanism in view of the soil particle rearrangement of granular thermodynamics. Comput Geotech 2021;137:104272. https://doi.org/10.1016/j.compgeo.2021.104272.

[38] Monismith C, Ogawa N, Freeme C. Permanent deformation characteristics of subgrade soils due to repeated loading. Transp Res Rec 1975;537:1–17.

[39] Li D, Selig ET. Cumulative plastic deformation for fine-grained subgrade soils. J Geotech Eng 1996;122:1006–13. https://doi.org/10.1061/(ASCE)0733-9410(1996)122:121006.

[40] Chai J-C, Miura N. Traffic-load-induced permanent deformation of road on soft subsoil. J Geotech Geoenviron Eng 2002;128:907–16. https://doi.org/10.1061/(ASCE)1090-0241(2002)128:11907.

[41] heng Shao, jun Zhi, dai Tang, xing Hong, qi Bing. Experimental study on cumulative deformation characteristics of coral sand under long-term cyclic loading. Chin J Geotech Eng 2019;41:161–4. https://doi.org/10.11779/CJGE2019S2041.

[42] Yesuf GY, Hoff I. Finite element modelling for prediction of permanent strains in fine-grained subgrade soils. Road Mater Pavement Des 2015;16:392–404. https://doi.org/10.1080/14680629.2015.1013053.

[43] Jafarian Y, Javdanian H, Haddad A. Dynamic properties of calcareous and siliceous sands under isotropic and anisotropic stress conditions. Soils Found 2018;58:172–84. https://doi.org/10.1016/j.sandf.2017.11.010.

[44] Lu D, Liang J, Du X, Ma C, Gao Z. Fractional elastoplastic constitutive model for soils based on a novel 3D fractional plastic flow rule. Comput Geotech 2019;105:277–90. https://doi.org/10.1016/j.compgeo.2018.10.004.

[45] Liu R, Hou H, Chen Y, Ming P, Zhu X. Elastoplastic constitutive model of coral sand considering particle breakage based on unified hardening parameter. Mar Georesour Geotechnol 2022;40:655–67. https://doi.org/10.1080/1064119X.2021.1924321.

[46] Zhang H, Luo Z, Qiu Y, Liu H, Gu J, Tang J. Experimental and mathematical modeling of monotonic behavior of calcareous sand. Adv Civ Eng 2020;2020:8861605. https://doi.org/10.1155/2020/8861605.

[47] Wang Z, Zhang L. Experimental study on dynamic parameters of calcareous sand subgrade under long-term cyclic loading. J Mar Sci Eng 2022;10:1806. https://doi.org/10.3390/jmse10121806.

[48] Ma W, Qin Y, Xu Z, Chen G. Prediction model for generation trend of axial deformation of saturated coral sand under cyclic loading. Soil Dynam Earthq Eng 2024;184:108861. https://doi.org/10.1016/j.soildyn.2024.108861.

[49] Peng W, Zhang J. Crushing and mechanical characteristics of coral sands under various stress paths. Mar Georesour Geotechnol 2024;42:1258–72. https://doi.org/10.1080/1064119X.2023.2265913.

[50] Niemunis A, Wichtmann T, Triantafyllidis Th. A high-cycle accumulation model for sand. Comput Geotech 2005;32:245–63. https://doi.org/10.1016/j.compgeo.2005.03.002.

[51] Wichtmann T, Triantafyllidis Th, Späth L. On the influence of grain shape on the cumulative deformations in sand under drained high-cyclic loading. Soils Found 2019;59:208–27. https://doi.org/10.1016/j.sandf.2018.11.001.

[52] Wang Z, Zhang L. Experimental study on dynamic parameters of calcareous sand subgrade under long-term cyclic loading. J Mar Sci Eng 2022;10:1806. https://doi.org/10.3390/jmse10121806.

[53] Indraratna B, Sun Y, Nimbalkar S. Laboratory assessment of the role of particle size distribution on the deformation and degradation of ballast under cyclic loading. J Geotech Geoenviron Eng 2016;142:04016016. https://doi.org/10.1061/(ASCE)GT.1943-5606.0001463.

[54] Alnedawi A, Nepal KP, Al-Ameri R. New shakedown criterion and permanent deformation properties of unbound granular materials. J Mod Transp 2019;27:108–19. https://doi.org/10.1007/s40534-019-0185-2.

[55] Shiau SH, Yu HS. Shakedown analysis of flexible pavements. Dev Theor Geomech 2000:643–653\r761.

[56] Sheng-Horng S. Numerical methods for shakedown analysis of pavements under moving surface loads. University of Newcastle; 2001.

[57] Chen G, Liang K, Zhao K, Yang J. Shear modulus and damping ratio of saturated coral sand under generalised cyclic loadings. Geotechnique 2024;74:116–33. https://doi.org/10.1680/jgeot.21.00181.

[58] He S-H, Zhi D, Sun Y, Goudarzy M, Chen W-Y. Stress–dilatancy behavior of dense marine calcareous sand under high-cycle loading: an experimental investigation. Ocean Eng 2022;244:110437. https://doi.org/10.1016/j.oceaneng.2021.110437.

[59] Galindo R, Patino H, Melentijevic S. Hysteretic behaviour model of soils under cyclic loads. Acta Geophys 2019;67:1039–58. https://doi.org/10.1007/s11600-019-00313-2.

[60] Li X, Fan G. On strain localization of Aeolian sand in true triaxial apparatus. Acta Geotech 2024;19:3115–28. https://doi.org/10.1007/s11440-024-02273-4.

[61] Zhang J, Cao J, Huang S. Effects of initial shear stress and vibration frequency on the dynamic pore-water pressure of saturated sands. Adv Civ Eng 2018;2018:6124809. https://doi.org/10.1155/2018/6124809.

[62] Ding X, Luo Z, Ou Q. Mechanical property and deformation behavior of geogrid reinforced calcareous sand. Geotext Geomembranes 2022;50:618–31. https://doi.org/10.1016/j.geotexmem.2022.03.002.

[63] Indraratna B, Thakur PK, Vinod JS. Experimental and numerical study of railway ballast behavior under cyclic loading. Int J GeoMech 2010;10:136–44. https://doi.org/10.1061/(ASCE)GM.1943-5622.0000055.

[64] Zhuang X, Zhao H, Tao G, Wang J, Huang Y. Accumulated deformation and dynamic strength properties of weak expansive soil under cyclic loading. Rock Soil Mech 2020;41:3192–200. https://doi.org/10.16285/j.rsm.2019.2180.

[65] Wang S, Lei X-W, Meng Q-S, Xu J-L, Xie L-F, Li Y-J. Influence of particle shape on the density and compressive performance of calcareous sand. KSCE J Civ Eng 2020;24:49–62. https://doi.org/10.1007/s12205-020-0145-8.

[66] Cao Z, Chen J, Cai Y, Zhao L, Gu C, Wang J. Long-term behavior of clay-fouled unbound granular materials subjected to cyclic loadings with different frequencies. Eng Geol 2018;243:118–27. https://doi.org/10.1016/j.enggeo.2018.06.019.

[67] Yuan B, Huang Q, Xu W, Han Z, Luo Q, Chen G, et al. Study on the interaction between pile and soil under lateral load in coral sand. Geomech Energy Environ 2025;42:100674. https://doi.org/10.1016/j.gete.2025.100674.

[68] Cabalar AF, Hasan RA. Compressional behaviour of various size/shape sand–clay mixtures with different pore fluids. Eng Geol 2013;164:36–49. https://doi.org/10.1016/j.enggeo.2013.06.011.

[69] Zhang T, Zhang C, Zou J, Wang B, Song F, Yang W. DEM exploration of the effect of particle shape on particle breakage in granular assemblies. Comput Geotech 2020;122:103542. https://doi.org/10.1016/j.compgeo.2020.103542.

[70] Huang M, Yao Z. Explicit model for cumulative strain of saturated clay subjected to cyclic loading. ytgcxb 2011;33:325.

[71] Hardin BO. Crushing of soil particles. J Geotech Eng 1985;111:1177–92. https://doi.org/10.1061/(ASCE)0733-9410(1985)111:101177.

[72] Einav I. Breakage mechanics—part I: theory. J Mech Phys Solid 2007;55:1274–97. https://doi.org/10.1016/j.jmps.2006.11.003.

[73] Qin Y, Du X, Wu Q, Ma W, Chen G. Experimental investigation of cyclic failure mechanism of saturated coral sand under various consolidation conditions. Bull Eng Geol Environ 2023;82:216. https://doi.org/10.1007/s10064-023-03245-w.